



Modelling microscale impacts assessment of urban expansion on seasonal surface urban heat island intensity using neural network algorithms

Milan Saha ^{a,b,1}, Abdulla - Al Kafy ^{c,1}, Arpita Bakshi ^d, Abdullah-Al- Faisal ^e, Abdulaziz I. Almulhim ^f, Zullyadini A. Rahaman ^{g,*}, Abdullah Al Rakib ^h, Md. Abdul Fattah ^d, Kaniz Shaleha Akter ^h, Muhammad Tauhidur Rahman ^{c,i}, Maomao Zhang ^j, R. Rathi ^k

^a Department of Urban & Regional Planning, Bangladesh University of Engineering & Technology (BUET), Dhaka, Bangladesh

^b School of Environmental Science and Management, Independent University, Bangladesh

^c Department of Geography & the Environment, The University of Texas at Austin, Austin, TX 78712, USA

^d Department of Urban and Regional Planning, Khulna University of Engineering and Technology, Khulna, Bangladesh

^e Department of Applied Geographical Information Systems and Remote Sensing, University of Southampton, SO17 1BJ, Southampton, United Kingdom

^f Department of Urban and Regional Planning, College of Architecture and Planning, Imam Abdulrahman Bin Faisal University, P.O. Box 1982, Dammam 31451, Saudi Arabia

^g Department of Geography & Environment, Faculty of Human Sciences, Sultan Idris Education University, Tanjung Malim 35900, Malaysia

^h Department of Urban & Regional Planning, Rajshahi University of Engineering & Technology (RUET), Rajshahi 6204, Bangladesh

ⁱ Department of City and Regional Planning, King Fahd University of Petroleum & Minerals, KFUPM Box 5053, Dhahran 31261, Saudi Arabia

^j College of Public Administration, Huazhong University of Science and Technology, Wuhan 430079, China

^k School of Information Technology and Engineering, Vellore Institute of Technology, Vellore, India

ARTICLE INFO

Article history:

Received 13 June 2022

Revised 20 August 2022

Accepted 3 September 2022

Available online 10 September 2022

Keywords:

Infrastructural development

Green cover

Urban heat island

Land surface temperature

Cellular Automation (CA) model

ABSTRACT

Investigation of surface urban heat island (SUHI) results from rapid urbanization and upsurge of land surface temperature (LST) has substantial socioeconomic and environmental impacts. This study investigates and simulates the impacts of rapid urbanization on LST and SUHI patterns in Sylhet City, Bangladesh, from 1995 to 2030. Landsat images and machine learning algorithms have been used to identify the urban growth, LST and UHI distribution patterns in several city directions. In addition, correlation analysis has been conducted between LST, SUHI and spectral indices (NDBI, NDBSI, NDVI, NDWI). Results suggested that urban expansion increased LST by 7 °C in summer and 6 °C in winter from 1995 to 2020. Increment has also occurred in summer high SUHI from 0.25 km² to 2.65 km². Pearson correlation demonstrated that built-up areas have a strong positive relationship with LST (0.96) and SUHI (0.911). Future simulation of urban expansion for 2025 and 2030 shows a 9 % increase, leading to a significant increase in moderate to high SUHI intensity. The study's findings can act as an effective guideline for sustainable infrastructural development and ensure environmental stability by increasing the thermal comfort level of the city.

© 2022 Elsevier B.V. All rights reserved.

1. Introduction

Urbanization is considered the engine of growth and development of any geographical location. The urban sectors of many emerging countries contribute significantly more to the gross domestic product (GDP) than the neighboring rural sectors. That is why developing countries are going through rapid and

unplanned urbanization, infrastructural construction, and industrialization for fast economic development [1,2]. Due to rapid urbanization, the urban population will reach five billion by 2030 [3,4]. The modification of land use/land cover (LULC) will attract more people to migrate into urban areas. Hence, it will further accelerate more modifications of LULC to serve different services to its increasing population. Cities will face more remarkable climates,

* Corresponding author at: Department of Geography & Environment, Faculty of Human Sciences, Sultan Idris Education University, 35900 Tanjung Malim, Malaysia.

E-mail addresses: milansaha023@gmail.com (M. Saha), abdulla-al.kafy@localpathways.org (Abdulla - Al Kafy), arpitabakshi36@gmail.com (A. Bakshi), abdullah-al-faisal@localpathways.org (Abdullah-Al- Faisal), aialmulhim@iau.edu.sa (A.I. Almulhim), zully@fsk.upsi.edu.my (Z.A. Rahaman), abdullahalrakib310@gmail.com (A. Al Rakib), mafattah.kuet@gmail.com (M.A. Fattah), mtr@kfupm.edu.sa (M.T. Rahman), star_mzhang@mails.ccnu.edu.cn (M. Zhang).

¹ These authors contributed equally to this work and are considered joint first authors.

ecosystems, and built-environment changes than the rural areas [5,6]. This remarkable difference in climatic change will accelerate the urban heat island (UHI) formulation and its impacts on urban areas. The UHI is gaining the attention of policymakers, scientific communities, urban planners, transportation engineers, and health authorities due to its substantial impacts on the living conditions of urban residents, air and water pollution, ecosystem modifications and increased energy consumption [7,8]. For ensuring a sustainable urban environment by adapting effective mitigation strategies, understanding the magnitude and extent of UHIs induced by expected urban expansion is crucial, especially in emerging cities.

The variation of temperature between urban land and the adjacent rural regions is a notable phenomenon in urban climates. The term UHI refers to noticeable temperature disparities [9]. Researchers identified two types of UHI: one is air UHI (measured based on the atmospheric temperature from the installed field weather stations and the other is SUHI (surface UHI, measured from surface temperatures) [10]. Because climate varies spatially and thermometers are not everywhere, measuring air UHI is complex and difficult for large geographical areas [12]. On the other hand, SUHI can allow one to characterize the UHI variations for any geographical region on a local or regional scale. Moreover, this allows the study of the influence of different factors on UHI for any geographical location and the consequences of UHI effects [12]. Therefore, this study focused on the SUHI on a large scale.

The influence of urbanization on the SUHI has been widely studied in prior research [7,13]. Researchers used several indicators like population density, surface area, and building density to characterize the urban SUHI [14,15] and employed both statistical [16,17] and numerical [18,19] models for simulating SUHI in different urban expansion scenarios. Rapid population growth and unplanned urbanization lead to the modification of LULC types, particularly the increase of built-up land cover areas and diminish of the rest of LULC types, such as greenery and water bodies absorb atmospheric carbon [20]. The modification of urban LULC types and urban activities, therefore, decreases forest land, greenery, crop land, as well as waterbodies and increases built-up areas. The loss of greenery and waterbodies is hampering carbon sequestration and attenuating global warming. This modification is causing drastic changes in the land surface temperature (LST) [21], further resulting in substantial climate change and SUHI effects [22]. Moreover, anthropogenic temperature release [23], reduction of windspeed [24], increase in energy consumption [25], traffic congestion and increase in vehicular activities [26] resulting from urbanization accelerate UHI effects. Prior studies showed the relationship between SUHI and LULC change [11,27]. So far, no detailed study has been conducted on the practical applications and theoretical achievement in the association between SUHI and urban surface modification in the eastern region of Bangladesh. Moreover, this hot topic has found less attraction in emerging cities.

To characterize intra-urban and peri-urban LULC change and identify urban expansion, the researchers use GIS and remote sensing (RS) techniques. Currently, the LULC classification technique is more advanced due to the application of machine learning algorithms. Previous studies showed the spatiotemporal LULC change and transformation. Current studies of LULC classification put more focus on using machine learning algorithms to simulate future potential land use patterns and their environmental impacts. In this regard, the Artificial Neural Network (ANN), Urban Growth Potential model, Frequency Ratio model, and Fuzzy Logic model have demonstrated higher accuracy in prediction results by integrating GIS and RS techniques [29–31]. Among these, the ANN-based Cellular Automation (CA) approach is used to compute the urban growth efficiently and has the highest spatial resolution,

which can simulate the future urbanization pattern with the influence of historical growth trends and the interactions between land-uses [31,32]. The ANN-based CA model integrates several models, enabling higher accuracy in predicting spatio-temporal patterns. Moreover, this model uses comparatively simple datasets that are easy to perceive, and the results are unambiguous to comprehend.

Althoug prediction of the future changing pattern of LULC and LST is a conventional approach, detailed prediction studies of seasonal SUHI dynamics influenced by LULC change are a new concept and have been studied in an insufficient number of studies. Considering the above circumstances, this study investigated the detailed responses of seasonal SUHI variations to rapid urbanization and predicted the future potential urban growth, LST, and UHI pattern of the study area. The study hypothesizes that there are adverse effects of land cover modification on the SUHI in urban areas and will answer the following research questions:

- i) How does the UHI respond to the urban expansion in Sylhet City from 1995 to 2020?
- ii) What are the causes of spatiotemporal variability in SUHI due to urbanization?
- iii) How will the future urban growth pattern and LST distributions of 2025 and 2030 contribute to the UHI variations in Sylhet City?

In the answers to these research questions, this study aims to estimate the.

- i. scenario of urban growth, LST and UHI for the last 25 years
- ii. directional analysis of urban expansion, LST and UHI distribution in the study area
- iii. relationship between LULC indices (NDVI, NDBI, NDBSI and NDWI) and LST as well as UHI.
- iv. LST and UHI distribution over different LULC classes
- v. prediction of future urban growth, LST and UHI pattern of the study area.

This study will play a useful role in identifying the impacts of urban expansion on UHI, which will help the city authority develop mitigating measures and management strategies, particularly in response to the projected extreme climate conditions.

2. Materials and methods

2.1. Study area

Sylhet is a metropolitan city located in northeastern Bangladesh and is the administrative center of Sylhet, Habiganj, Sunamganj, and Moulvibazar districts. The city is characterized by the hilly areas and river basins which have made it one of Bangladesh's most distinctive places, located between 24.8917°N and 91.8833°E. About 0.50 million people live in an area of 26.57 km² with 1.73 % growth rate, annually. There are three distinct seasons in Sylhet, namely: summer (March to June), the rainy season (July to October), and the winter season (November to February). Hot and humid tropical monsoon is also featured between April and October. The total rainfall is 4200 mm for which 80 % has occurred during May to October [33]. The average annual temperature in SCC is 29.6 °C and the average temperature ranges between 25.20 °C and 27.10 °C in winter, between 30.40 °C and 30.90 °C in summer, and between 28.33 °C and 27.77 °C in the rainy season [34].

SCC in Fig. 1 is considered one of the most economically advantageous and ecologically sound cities in Bangladesh after the cap-

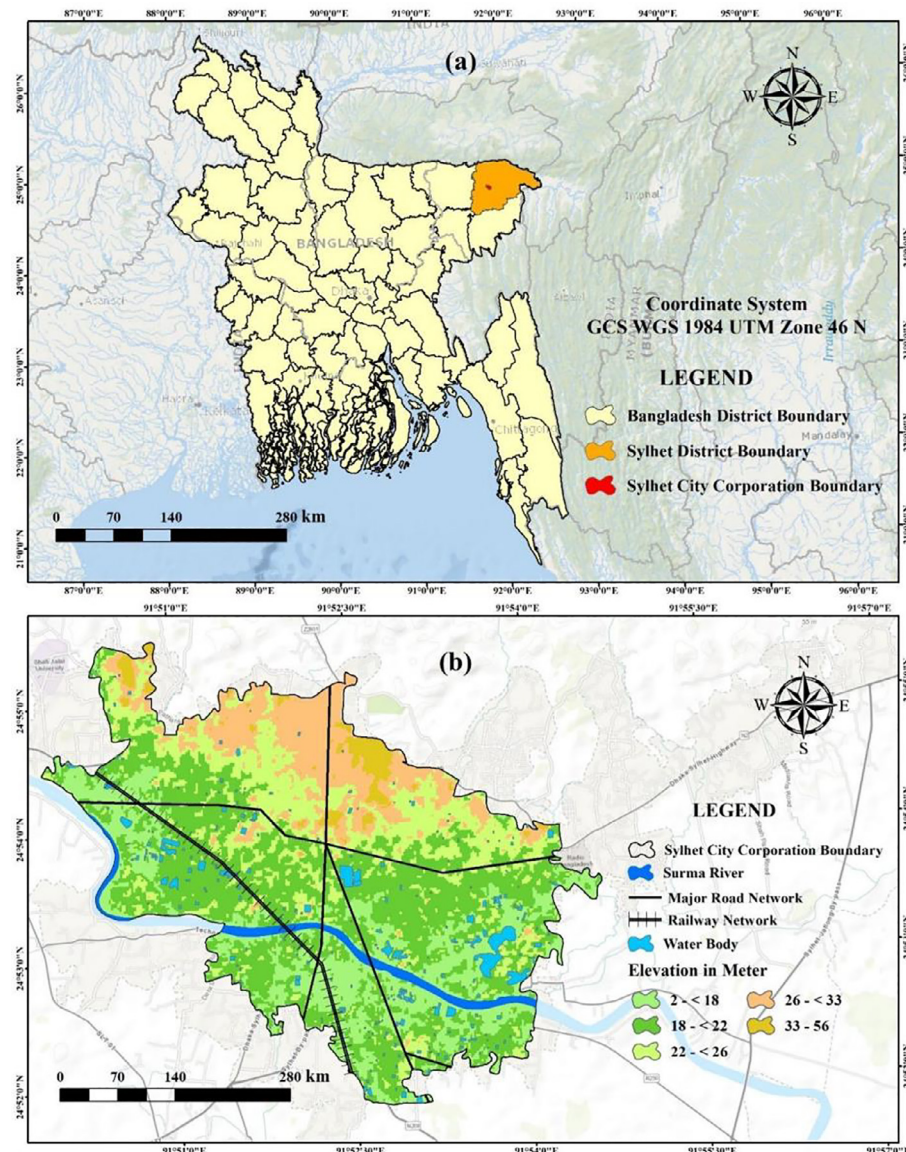


Fig. 1. Location map of the study area (a) Bangladesh (b) Sylhet City Corporation.

ital city of Dhaka and the commercial capital, Chittagong City. The city's major economic drivers are the tea industry, religious tourism, natural gas fields and industries, crude oil, and rice production. Many roads were constructed to connect the Sylhet division with other cities, and this helped expand the tea industry in the last century. Rapid urbanization took place in the town (which formed SCC in 2001) during 1950–1960, aided by the expatriate Sylhetis, and the process is currently underway. In recent years, the influence of the economic condition has led to rapid infrastructural and socioeconomic development in the SCC area. The SCC received a significant share of the annual remittances of the country, which accelerated the expansion of real estate and construction (SCC, 2022). Moreover, different city centers and improved service facilities attracted the migration of rural people to SCC. As a result, the city has been facing rapid LULC change, including the construction of roads, buildings, and other infrastructure, and this LULC change has been accelerated mostly in the last few decades. But, like other cities in Bangladesh, SCC is also facing unplanned and rapid urban expansion, which may have further severe environmental effects. That's why this study considered SCC as the study area.

2.2. Datasets

Twelve (six for each season) multispectral Landsat satellite data were acquired from US Geological Survey (USGS) website (<https://www.earthexplorer.usgs.gov>). Month-based timeline was followed during the acquisition process to maintain the seasonal similarity among the database for each season from 1995 to 2020 with a five-year interval among the data. Landsat 4–5 TM was considered for the year before 2010 and for 2015 and 2020, Landsat 8 OLI was used. Different land cover indices like NDVI, NDBI, NDBSI, and NDWI was calculated to view the in-depth LULC change pattern during the study period. All the images followed the same path/row, i.e., 136/43, and all the images had <10 % cloud coverage (Table 1). Detail methodological process is illustrated in Fig. 2.

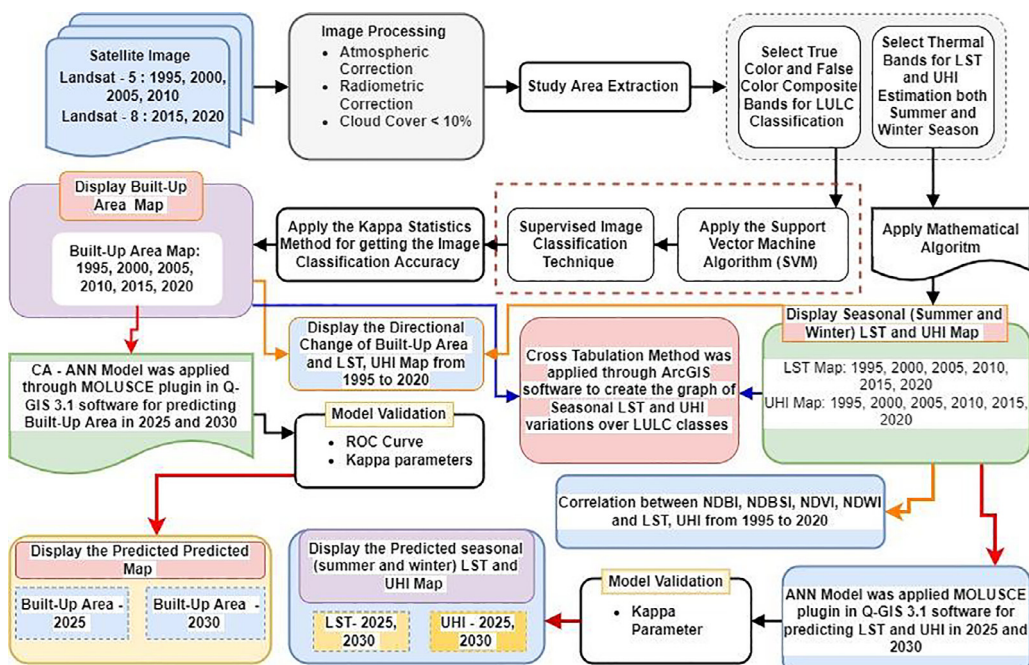
2.3. Estimation of urban expansion

Different directional observation of urban expansion is one of the most recurrent techniques in examining the speed of urbanization in those directions. Visual input of heterogeneous urban growth in separate directions helps differentiate expansion rate

Table 1

List of Landsat images downloaded from USGS.

Season	Month	Year	Scene ID	Sensor	Cloud Cover	Path / Row
Summer Season (March to June)	March	1995	LT51360431995078ISP00	Landsat 4-5TM	<10 %	136/43
	March	2000	LT51360432000094BKT01		<10 %	136/43
	May	2005	LT51360432005121BKT00		<10 %	136/43
	May	2010	LT51360432010135KHC00	Landsat 8 OLI	<10 %	136/43
	March	2015	LC81360432015069LGN01		<10 %	136/43
	May	2020	LC81360432020131LGN00		<10 %	136/43
Winter Season (December to February)	January	1995	LT51360431995030BKT00	Landsat 4-5TM	<10 %	136/43
	February	2000	LT51360432000060BKT00		<10 %	136/43
	February	2005	LT51360432005041BKT00		<10 %	136/43
	January	2010	LT51360432010023KHC00	Landsat 8 OLI	<10 %	136/43
	January	2015	LC81360432015002LGN01		<10 %	136/43
	January	2020	LC81360432020019LGN00		<10 %	136/43

**Fig. 2.** Flow diagram of the methodological process for the study.

in individual sectors [35]. 30 km, multiple ring buffer was created around the city center, covering all the urban areas. For micro-scale observation, the buffer structure was segregated into 16 equal parts, creating 16 different directional input in the analysis.

Speed and intensity, are two main factors to examine the directional urban increase and the indices related to these factors help define the increasing pattern in different timelines (Liu and Bu, 2000; Xu and Chen, 2004). These two equations are the calculative approach defining the speed and intensity indices.

$$M_{ue} = \frac{\Delta U_{ij}}{\Delta t_j \times ULA_{ij}} \times 100\% \quad (1)$$

$$I_{ue} = \frac{\Delta U_{ij}}{\Delta t_j \times TLA_{ij}} \times 100\% \quad (2)$$

Here,

M_{ue} = Expanding Speed Index.

I_{ue} = Expanding Intensity Index.

ΔU_{ij} = A certain directional urban expansion zone (i for zone, j for period).

Δt_j = Time-span.

ULA_{ij} = The total amount of urban area for study region i and period j.

TLA_{ij} = The total amount of urban area for the study region i.

A trend-based output of urban expansion scenario during many study periods can be easily observed with the expansion speed. But to standardize the increasing rate compared to other spatial features, the expanding intensity index is used [36].

The center of gravity, on the other hand, is a prominent indicator describing the transition of a geographical subject [37,38] that resembles the spatial distribution of a spatial feature, the overall difference between land covers and the concentration of each spatial feature and its' dynamic conversion, specifying the directional picture. To correlate the urban development with related policies and strategies, gravitational center is considered as a useful index regarding urban area.

For multiple spatial inputs, the following equation can reveal the coordinates of gravity center.

$$X_t = \frac{\sum_{i=1}^n (C_{ti} \times X_i)}{\sum_{i=1}^n C_{ti}} \quad (3)$$

$$Y_t = \frac{\sum_{i=1}^n (C_{ti} \times Y_i)}{\sum_{i=1}^n C_{ti}} \quad (4)$$

Here, $X_t = Y_t$ = the gravity center of the urban area at the time t. $X_i = Y_i$ = the coordinate of the geometric center of the urban area in I block.

C_{ti} = Area of I block.

Two main variables were considered, i.e., gravity center travel distance (L) and gravity center transfer angle (α), where L resembles the similarity of urban areas in different time periods and α shows the higher concentrated urban signatures [37,38].

$$L_{t+1} = \sqrt{(x_{t+1} - x_t)^2 + (y_{t+1} - y_t)^2} \quad (5)$$

Here, L_{t+1} means the transfer distance of the gravity center between period t and t + 1.

$$\begin{aligned} \alpha_{t+1} = & \left\{ \arctan \arctan \left(\frac{y_{t+1} - y_t}{x_{t+1} - x_t} \right), x_{t+1} \geq x_t, y_{t+1} \right. \\ & \geq y_t, \pi - \arctan \arctan \left(\frac{y_{t+1} - y_t}{x_{t+1} - x_t} \right), x_{t+1} < x_t, y_{t+1} \\ & \geq y_t, \pi + \arctan \arctan \left(\frac{y_{t+1} - y_t}{x_{t+1} - x_t} \right), x_{t+1} < x_t, y_{t+1} \\ & < y_t, 2\pi + \arctan \arctan \left(\frac{y_{t+1} - y_t}{x_{t+1} - x_t} \right), x_{t+1} \geq x_t, y_{t+1} < y_t, \end{aligned} \quad (6)$$

α_{t+1} resembles the angle between east and the transfer direction from time t to t + 1.

2.4. The extraction of seasonal spatiotemporal distribution of LST

Two types of Landsat images were acquired for retrieving the temperature of the study area for a certain period of time. Thermal band 6 was extracted from Landsat 4–5 TM and 10 and 11 thermal band of Landsat 8 OLI were used for precise computation of LST.

In the primary stage, the spectral radiance (λ) was computed using the following equations.

$$L_\lambda(\text{for landsat 5}) = L_{min} + \frac{L_{max} - L_{min}}{Qcal_{max} - Qcal_{min}} \times DN \quad (7)$$

$$L_\lambda(\text{for landsat 8}) = ML \times DN + AL \quad (8)$$

Here, ML refers to a multiplicative rescaling factor having a value of 0.0003342 and AL resembles an additive factor having a value of 0.1. Each of these factors are band specific [39].

$$\rho = \frac{h \times c}{\sigma} = 1.438 \times 10^{-2} mK$$

Here,

h = Plank's constant = 6.626×10^{-34} Js.

c = velocity of light = 2.998×10^8 ms $^{-2}$.

σ = Boltzmann constant = 5.67×10^{-8} Wm 2 k $^{-4}$ = 1.38×10^{-23} JK $^{-1}$.

$$T_B = \frac{K_2}{\ln \ln \left(\frac{K_2}{L_\lambda} + 1 \right)} \quad (9)$$

T_B = satellite brightness temperature.

K_1 and K_2 have individual values for Landsat 4–5 TM and Landsat 8 OLI. For Landsat 4–5 TM, K_1 and K_2 values are 607.7 and 1260.6 respectively and for Landsat 8 OLI, the values are 774.9 and 321.07 for K_1 and K_2 respectively [41–43].

Using all of these values, the LST was calculated using the following equation.

$$LST = \frac{T_B}{1 + \left(\lambda \times \frac{T_B}{\rho} \right) \times \ln \ln (\varepsilon)} \quad (10)$$

Here, ε = land surface emissivity, ranging between 0.97 and 0.99 [44,45].

2.4.1. Accuracy measurement of the estimated LST

To validate the estimated LST, Landsat data and station data from BMD (Bangladesh Metrological Department) of Sylhet station were collected for both summer and winter seasons from 1995 to 2020 (Fig. A.1 (a-b)). (Fig. A.1 (a)) represents a high degree of R-square (>0.90) value for all the selected years that portrays maximum similarity between extracted LST data from Satellite and BMD for summer. A high R-square value was observed for 2010 among all. The winter season also recorded high value (Fig. A.1 (b)). It clearly indicates the consistency of retrieved satellite LST and station data.

2.5. Estimation of UHI ratio index (URI)

The spatiotemporal variation of UHI effect was computed using the LST data retrieved from satellite images [46,47].

The comparative concentration of LST based on the surrounding area reveals the UHI phenomena of the respective area. Rural areas should be also be taken into account to successfully understand the UHI effect on the surroundings [48,49]. During the course of time, only the LST value changes in a remote sensing dataset, rather than changing the entire spatial distribution. Therefore, normalizing the spatial distribution for an appropriate comparison is necessary [35]. For normalizing, the following equation was used,

$$T_n = \frac{LST - T_{min}}{T_{max} - T_{min}} \quad (11)$$

Here,

T_n = Normalized Raster.

T_{max} = Maximum LST value.

T_{min} = Minimum LST value.

Density-based segregation was followed in the normalized LST raster with five classes, i.e., low, semi-medium, medium, semi-high, and high. Finally, URI approach was taken to measure the urban land impact in the UHI phenomena using the following equation.

$$URI = \frac{1}{100m} \sum_{i=1}^n \omega_i p_i \quad (12)$$

Here, m = number of normalized temperature level.

i = number of comparatively higher temperatures than rural areas.

n = number of higher temperature levels concentrated in urban lands.

ω = weighted value with respect to i.

p = percentage of area in level i.

Considering the weighted value of the temperature of each level, the ratio of UHI area to urban land is regarded as URI, the shows the UHI growth concentration in urban areas. A higher value in URI generally reveals a greater risk scenario of UHI in the respective area.

2.6. Directional changes estimation of urban expansion, LST, and UHI

A directional overview of a temporal changing phenomenon helps one to comprehend the distribution of the respective features spatially, in a microscopic way. Many researchers included

the importance of this approach in their papers and showed a certain degree of influence of that approach [50,52]. An urban center was detected, and rings were drawn surrounding the city core at 200 m intervals. Considering 16 gradient directions, the rings were divided into 16 equal sections, representing 16 individual directional distributions. Finally, the data and observation layer intersected, which portrays the maximum percentage of built-up area for each segment.

2.7. Predicting the future LULC scenario

The Cellular Automation (CA) model can simulate the future urban expansion scenario, implying the probabilities of land use transition by ANN learning process. The MOLUSCE plugin in QGIS 2.18 was used, having six phases of the prediction process.

Firstly, to build the algorithm, maps of 1995 and 2000 were used, including factors like DEM, aspect map, slope map, Euclidean distance from road and rivers, and urban footprint concentration, to measure spatial variation. With that, the changing pattern for 2005 and 2010 was simulated. The same projected coordinate system and spatial resolution like the classified maps were maintained throughout the process. The process consisted of calculating percentile area change and creating a transition matrix revealing the ratio of shifting pixels within land cover classes. An aerial transformation map for the simulation years was also created during this process. Then, the ANN (Multi-layer perceptron) model was used to predict the 2005 and 2010 scenarios [53,54].

Pearson's correlation, Uncertainty of Joint information, Crammer's V were used to examine the correlation among the spatial variable factors in two raster images [55]. The transition matrix is then calculated using a real change between initial and the final year as a base [56,57]. Different prediction models are used among researchers to produce potential transition maps, such as ANN, Weights of Evidence (WoE), Logistic Regression (LR), and Multi-criteria Evaluation (MCE). Every methodology is involved with taking LULC and geographic factors as input [58,59]. After predicting and comparing with the real classified maps, kappa coefficient measures were followed.

On the other hand, ANN approach involves using previous data in every prediction step, creating a transition matrix. Uncertainty and high amount of variable input are handled expertly by this model. A continuous process is then created by signifying the terrain with a value ranging between 0 and 1. Because of fuzzy logic requirements, terrain usability helps define the incessant range. The core feature of ANN is mainly the interaction among linked neurons and the weight connections between them [60].

The validation process involved with both kappa statistics and ROC curves. Comparing the real-life LULC raster and the predicted map of the same year, the overall kappa value was calculated using the equation below:

$$K_{value} = \frac{p_0 - p_e}{1 - p_e} \quad (13)$$

p_0 = the proportion of actual agreement. = $\sum_{i=1}^c p_{ij}$

p_e = the proportion of expected agreement = $\sum_{i=1}^c (p_i T \times p T_j)$

p_{ij} = i^{th} and j^{th} cell in the contingency table.

$p_i T$ = sum of all cells in the i^{th} row.

$p T_j$ = sum of all cells in the j^{th} column.

c = raster category count.

The frequency overview is observed with the contingency table and is used in this study to reveal the interrelation between i^{th} and j^{th} cell.

ROC (Receiver Operating Curve) curve, a binary classifier, illustrated the model performance and involved in trading off between true positive rate and false positive rates to validate projected land uses and reference data. AUC (Area under Curve) value indicated the model's usefulness by summarising the test's overall accuracy. This AUC value is basically ranging from 0 to 1 where 0.50 represents no discrimination, 0.7 to 0.8 depicts acceptable, 0.8 to 0.9 and above 0.9 as excellent and outstanding performance respectively [61].

2.8. Predicting the future LST and UHI distribution

500 m × 500 m spatial grid was used in QGIS interface to observe the changing pattern significantly, R^2 [62]. Centroid coordinates and the mean of those pixel values for a spatial feature was of the few inputs in the ANN model. In LST prediction phase, parameters like previous LST distribution patterns, land cover indices like NDBI, NDBSI of the five-year interval,

latitude and longitude were served as inputs to examine the hidden pattern among the dataset to simulate the future distribution scenario [64]. A similar approach was taken for seasonal UHI prediction for the same year, with LULC, LST, UHI, NDBI, NDBSI, latitude, and longitude as input parameters [51]. The following three equations can derive the mathematical expression of those above discussions:

$$LST(t+5) = f[LST(t), LST(t-5), LULC(t), LULC(t-5), NDBI(t), (t-5), NDBSI(t), NDBSI(t-5)] \quad (14)$$

$$UHI(t+5) = f[LST(t), LST(t-5), UHI(t), UHI(t-5), LULC(t), FTLULC(t-5), NDBI(t), NDBI(t-5), NDBSI(t), NDBSI(t-5)] \quad (15)$$

The nonlinear behavior of the algorithm greatly depends on the hidden layers and neurons as these affect the predicted output, R^2 [62] and its' accuracy level. The seasonal LST and UHI were predicted using the hidden layers, having 1–3 times hidden neurons in each layer. ANN structure is mainly built with three layers, i.e., i, j, and k, meaning input, hidden, and output layers, respectively, with weights W_{ij} and W_{jk} . Each neuron comprises of a weight factor (w) and bias (b). The input value evaluated the weighted sum from the previous layers from each neuron [65]. For example, y in the second layer can be calculated with the following equation:

$$y_{pj} = \sum_{i=1}^l W_{ij} O_{pi} + \theta_j \quad (16)$$

Here, θ_j = bias for neuron j .

O_{pi} = the i^{th} output of the previous layer.

W_{ij} = weight between first and second layer.

Here, the y value enters into a nonlinear activation program, generating $f(y)$ from every second and third layer neuron. Usually followed equation to derive this logistic function is shown below [66]:

$$f(y) = \frac{1}{1 + e^{-y}} \quad (17)$$

The learning rate (μ) influences the time and number of approaches to be taken to achieve the adjustment in each multidimensional weight space [63]. Large μ indicates irregularities and slow convergence of minimum error value. Alternatively, small μ reveals the number of iterations to be too large to achieve the local minima [64,67,68]. Due to these complications, the primary μ rate was set to 0.1, controlling that with decay rate (β), which ranges from 0 to 1, but for this study was set to 0.9 for updating the μ . Any deterioration in the present and past iteration followed by β updating μ with multiplication. The opposite scenario, i.e., deviation occurred during the increment of the error function by reducing μ .

Table 2

Accuracy assessments table of the classified LULC maps.

Year	LULC Class	Validation points for different LULC classes					User Accuracy
		Bare Land	Built-up Area	Vegetation	Water Body	Total	
1995	Bare Land	68	2	1	1	72	94.44
	Built-Up Area	2	93	0	0	95	97.89
	Vegetation	3	1	80	1	85	92.31
	Water Body	2	0	1	45	48	93.75
	Total	75	96	82	47	300	
	Producer Accuracy	90.67	96.88	97.56	95.74	Overall Accuracy 95.34 %	Kappa Coefficient 93.66
2000	Bare Land	70	3	1	1	75	93.33
	Built-Up Area	4	83	2	1	90	92.22
	Vegetation	3	2	75	0	80	93.75
	Water Body	2	0	1	52	55	94.55
	Total	79	88	79	54	300	
	Producer Accuracy	88.61	94.32	94.94	96.30	Overall Accuracy 93.34 %	Kappa Coefficient 91.03
2005	Bare Land	77	2	1	0	80	96.25
	Built-Up Area	2	86	1	1	90	95.56
	Vegetation	2	1	67	0	70	95.71
	Water Body	1	1	2	56	60	93.33
	Total	82	90	71	57	300	
	Producer Accuracy	93.90	95.56	94.37	98.25	Overall Accuracy 95.34 %	Kappa Coefficient 93.73
2010	Bare Land	78	3	2	2	85	91.76
	Built-Up Area	1	86	2	1	90	95.56
	Vegetation	2	2	65	1	70	92.86
	Water Body	1	1	1	52	55	94.55
	Total	82	92	70	56	300	
	Producer Accuracy	95.12	93.48	92.86	92.86	Overall Accuracy 93.67 %	Kappa Coefficient 91.46
2015	Bare Land	77	3	2	0	82	93.90
	Built-Up Area	1	84	2	1	88	95.45
	Vegetation	3	1	69	2	75	92.00
	Water Body	2	0	2	51	55	92.73
	Total	83	88	75	54	300	
	Producer Accuracy	92.77	95.45	92.00	94.44	Overall Accuracy 93.67 %	Kappa Coefficient 91.47
2020	Bare Land	60	2	2	1	65	92.31
	Built-Up Area	1	91	2	1	95	95.79
	Vegetation	1	1	82	1	85	96.47
	Water Body	1	2	2	50	55	90.91
	Total	63	96	88	53	300	
	Producer Accuracy	95.24	94.79	93.18	94.34	Overall Accuracy 94.34 %	Kappa Coefficient 92.32

2.8.1. Accuracy assessment of predicted LST in CA-ANN model

Model accuracy is a vital issue in identifying the degree of reliability of that model with in-situ data. To assess the sensitivity between station data and the predicted LST by CA-ANN model, (Fig. A.2 (a-b)) represents the validation of the adopted model for the summer and winter seasons. Each diagram shows the high degree of association and precision of predicted and BMD LST data.

3. Result and discussion

3.1. LULC classification and change detection analysis

The supervised classification algorithm was utilized to generate LULC maps for 1995 to 2020 at five years intervals where the kappa coefficient values were above 90 % for all classified images (Table 2). Over the last 25 years, it has experienced a rapid urbanization process, whereas the percentage of built-up area has increased rapidly. From 2000 to 2020, the built-up area increased from 6.44 km² to 13.99 km² at the rate of 1.17 km² per year, covering half of the city corporation area as 52.66 % (Fig. 3).

Fig. 4(a-f) represents a rampant transition from other land-use classes to built-up area from 1995 to 2020. Built-up area was terribly increased (13.41 km²) by altering bear land and vegetation cover at a high percentage between 2015 and 2020. Almost 10 km² (40.67 %) of vegetation and bear land were decreased in the last 25 years. In contrast, comparatively less transformation was noticed in water bodies as 1.49 % (Fig. A.3). This refers to massive excavation and river bank preservation projects initiated by Sylhet city.

Both population density and elevation influence as driving forces for this notable urban area conversion [33]. Historically, urban concentration was mostly found on the bank of River Surma in the southern part up to 1991. But waterlogging and flood in lower elevation has driven the population to shift to higher elevation towards the north. Moreover, an extension of the territorial area, rural-urban migration, employment opportunities, and blooming development activities has contributed to the major transformation of SCC from other classes into built-up areas [52,69]. As a result, Sylhet is undergoing unplanned urbanization, which has placed an external load on the area's environmental sustainability [33,70,71].

3.2. Analysis of seasonal LST variations

Landsat imagery and RS applications with mathematical algorithm was applied to estimate reliable LST variation. Landsat thermal bands contributed in areal distribution of LST from 1995 to 2020 (Fig. 5). Higher temperature was observed in the core city in 1999, dramatically spreading to adjacent and outside of the city center from 2000 to 2020. Additionally, 32.06 °C and 36.27 °C were counted maximum temperature in summer 1995 and 2020 respectively at the rate of 0.13 °C per year. The lowest temperature in summer was 21.55 °C for 1995 and extended to 28.31 °C in 2020.

Areal distribution of LST was classified into six temperature classes in Table 3 for the summer season (1995, 2000, 2005, 2010, 2015 &2020). Most of the areas were under 18 °C - < 22 °C (6.10 %), 22 °C - < 26 °C (65.36 %), 26 °C - > 30 °C (28.14 %) and 30 °C - < 34 °C (0.40 %) temperature zones during summer 1995.

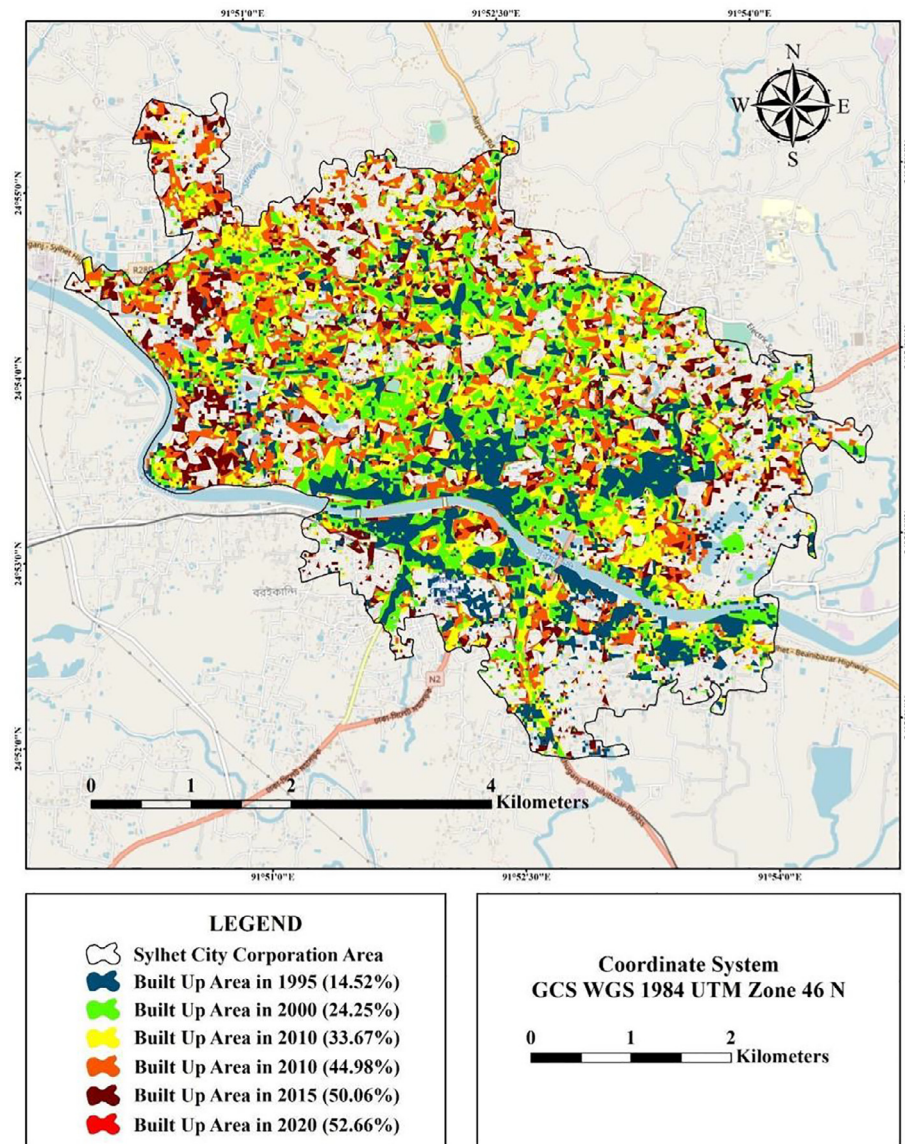


Fig. 3. Distribution of built-up area from 1995 to 2020.

22 °C - < 26 °C was recorded as the most prominent temperature class covering a 17.366 km² area in the following year. Meanwhile, the result showed that in summer 1995 to 2020, no area was recorded in the zone up to 18 °C. Therefore, 26 °C - 30 °C, 30 °C - 34 °C and > 34 °C covered 1.96 km² (7.38 %), 22.46 km² (84.55 %), 2.14 (8.08 %) respectively for summer 2020 (Fig. A.4). The highest temperature zone, > 34 °C was recorded no areas during 1995 and 2.15 km² for the year 2020 summer. It shows that the minimum temperate zones of 1995 tremendously converted into high temperate zones, especially between 2010 and 2020.

LST areal distribution maps for the winter season of 1995, 2000, 2005, 2010, 2015 and 2020 are illustrated in Fig. 5. Maximum temperature in winter 1995 was 19.61 °C and 25.26 °C for 2020. Winter LST distribution ranges from < 18 °C, 18 °C - < 22 °C, 22 °C - < 26 °C (Table 3). During 1995 to 2020, no area was recorded under 26 °C - < 30 °C, 30 °C - < 34 °C and > 34 °C zones. The most recorded areas were under < 18 °C (25.48 km²) in 1995 and 18 °C - < 22 °C (14.57 km²) in 2020. The highest temperature was recorded under the range of 18 °C - < 22 °C in the winter

1995, covering 4.10 % of area, whereas 22 °C - < 26 °C covered 45.17 % of the study area (Fig. A.4). The estimated result shows that there exists a huge fluctuation between summer and winter season temperature as the maximum temperature ended up to and started from 26 °C for winter 2020 and summer 2020 respectively. In winter, earth's tilt is away from the sun and the amount of solar radiation and sun angle are declined as a result of summer. These distributed rays reduce the amount of heat and reach out to the earth.

The significant increase in LST is the combined effect of population growth and acceleration of built-up areas. Built-up areas have less energy absorption capacity but massive thermal reflectance properties, increasing the LST and enhancing the thermal effect in urban areas [21]. The increasing built-up density near the bank of Surma River, Dhaka-Sylhet highway and Sunamganj-Sylhet highway is comparatively greater than any other region; therefore, the LST has increased in these specific regions over the year. This rising trend of LST speeds up the effects of UHI, affecting urban health and achieving sustainable urban areas [72].

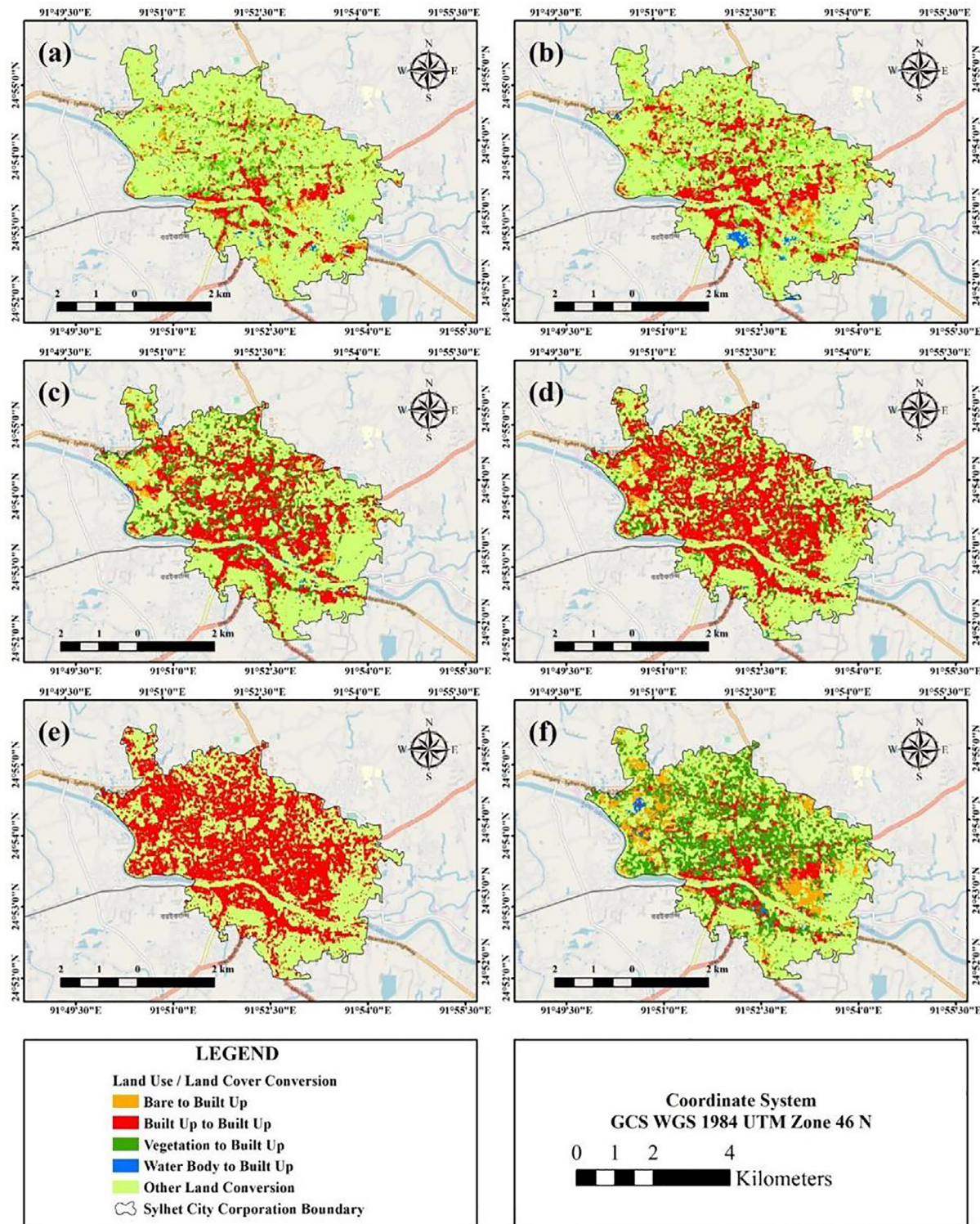


Fig. 4. Conversion of different LULC to built-up areas (a) 1995–2000 (b) 2000–2005 (c) 2005–2010 (d) 2010–2015 (e) 2015–2020 (f) 1995–2020.

3.3. Analysis of seasonal UHI distribution

The UHI exhibits the thermal conditions of a city, which is substantially warmer than the adjacent area as a result of various human infrastructure and activities in the urban area. Fig. 6 illustrates the UHI distribution of both summer and winter threshold values from 1995 to 2020.

The most observed UHI was recorded within the category of none (11.87 km^2) and very low (9.52 km^2) during summer 1995,

representing 44.70 % and 35.86 % of the total area, respectively. 3.24 km^2 (12.21 %), 5.26 km^2 (19.82 %), 5.65 km^2 (21.29 %) areas were recorded as low category UHI effect for 2000, 2005 and 2010, respectively (Table 4), whereas a declining trend was experienced by 18.59 % area in 2015 and 11.25 % in 2020 (Fig. A.5). UHI had high and very high impact on 2.65 km^2 and 1.62 km^2 area between 1995 and 2020 and very least impact (0–0.75) on 2.94 km^2 as well (Fig. A.6). Decreasing low impact value was replaced by high and very high UHI value in the city centre due

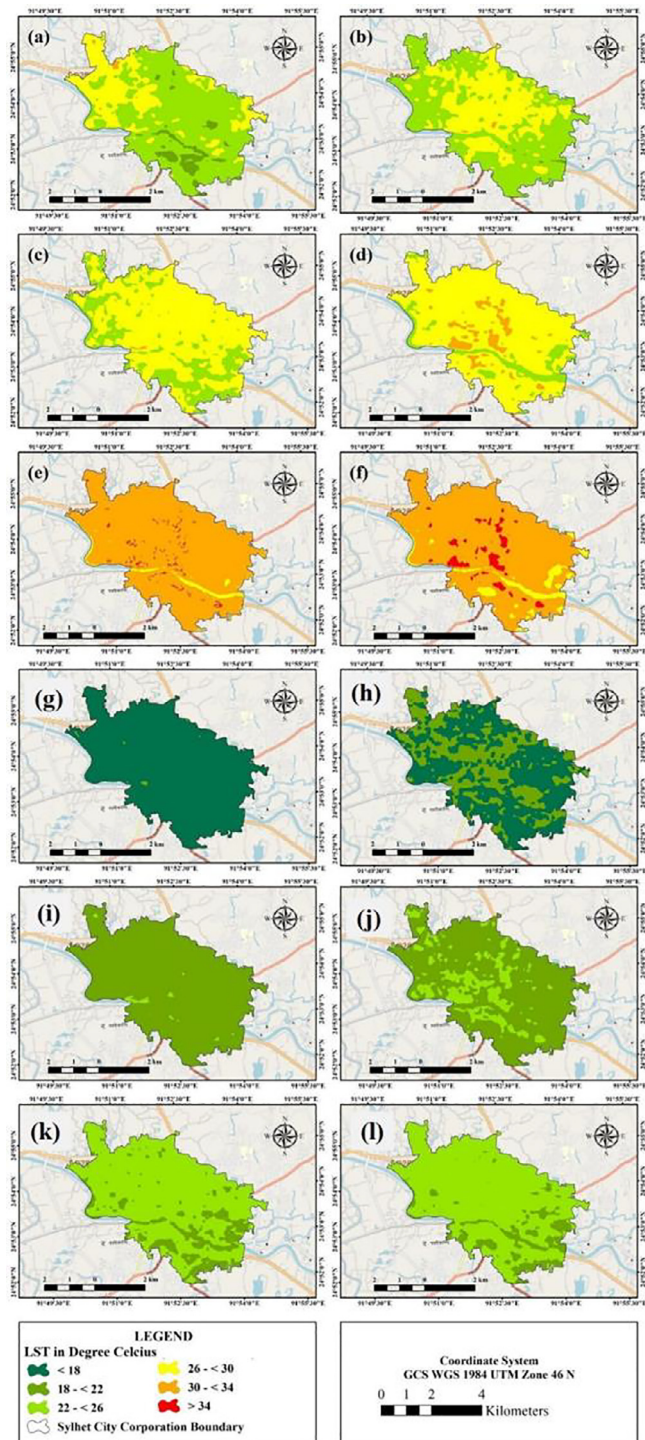


Fig. 5. Distribution of summer (a-f) and winter (g-l) LST in the study area (a) & (g) 1995 (b) & (h) 2000 (c) & (i) 2005 (d) & (j) 2010 (e) & (k) 2015 (f) & (l) 2020.

to high built-up density, large scale mega projects and infrastructure development.

In the winter (1995 to 2020), none and very low UHI effect decreased rapidly from 17.11 km^2 to 10.20 km^2 . Additionally, very low UHI was increased from 35.60 % to 49.08 % from 1995 to 2020 whereas low and moderate zones were enhanced from 0 % to 6.88 % and 5.64 %, respectively.

The distribution of seasonal UHI effects represents that none and very low UHI effects were declined over the years whereas low, moderate, high and very high zones increased significantly.

The none and very low zones are mostly suitable for living; therefore, higher UHI indicates a high thermal effect due to increasing impervious surface as well as vulnerable environmental effects [73].

3.4. Difference between atmospheric UHI and SUHI

The placement of the weather station are crucial for atmospheric UHI, which can be varied significantly even within the same urban area [74,75]. It is affected mostly by local climate condition and generally exists a substantial diurnal cycle [76]. At the height of 1.5 to 2 m, the air temperature is detected by making contact with the sensor and surrounding air [77]. However, LST is the good indicator for determining the energy balance and skin temperature of the land surface [78]. Heating and cooling effect of earth's surface are very rapid compared to air temperatures. Therefore, during midday, SUHI is experienced at a high rate, whereas the amount is huge for atmospheric UHI at night. Undulated topography, surface type of the urban area are the influencing factors for affecting LST and increasing the SUHI effect [75]. Additionally, the relationship between LST and atmospheric temperature is subjected by land use land cover changes over local or global level [79].

3.5. Directional change analysis of urban expansion

Directional change assessment is a popular technique to analyze and visualize urban land use changes in response to urban expansion [40]. To notify the urban area change direction, 16 gradient directions with 100-meter intervals were placed from core city to overall study area (Fig. 7).

The urban area was concentrated on east, southeast and near the Surma River towards southern direction in 1995. Except for the northern half of the study area, urban areas shifted in all directions between 1995 and 2000. Similar expansion pattern was also observed between 2000 and 2005. After 2010, the directional changes were quite prominent in the northwest, west and southwest part as Sunamganj – Sylhet highway has passed through the north-west zone of SCC. High elevation in the northern part led to the growth toward the study area's southern, eastern and western zone. Between 2015 and 2020, the highest expansion was occurred towards the northwest, western and southwest directions. It is anticipated that the southern part to be covered by impervious surface due to Dhaka – Sylhet highway has crossed over the southern zone of SCC area where massive urban development has been implemented.

Several projects have been initiated to develop Sylhet city; for example: Bangabandhu Sheikh Mujib Hi-Tech Park, Dhaka-Sylhet six-lane highway, Roads and drain expansion, Osmani-International airport expansion, Sylhet-Tamabil four-lane highway. Already implemented projects create employment opportunities and intensify buildup area conversion and expansion.

3.6. Directional changes of seasonal LST variations

Directional urban expansion is strongly associated with the directional change of both summer and winter season LST. Directional change of seasonal LST signifies the study area's emission of land surface thermal radiance for last 25 years (Fig. 8). In the summer of 1995, maximum directions were recorded under 22°C – 26°C and 26°C – $< 30^{\circ}\text{C}$ LST zones where 26°C – $< 30^{\circ}\text{C}$ was headed towards northwest part of the city. In 2000, 26°C – $< 30^{\circ}\text{C}$ zone was more concentrated in the city center and spreading all over the direction. Similar growth patterns except for the 30°C – $< 34^{\circ}\text{C}$ LST zone in the northeast and south-

Table 3Area (Km^2) wise LST distribution.

Year	Season	LST in Degree Celsius ($^{\circ}\text{C}$)					
		< 18	18 - < 22	22 - < 26	26 - < 30	30 - < 34	> 34
1995	Summer		1.622	17.366	7.476	0.106	
	Winter	25.480	1.090				
2000	Summer		0.148	15.401	10.628	0.393	
	Winter	17.288	9.282				
2005	Summer			7.585	17.192	1.793	
	Winter		21.888	4.682			
2010	Summer			2.92	21.661	1.989	
	Winter		17.785	8.785			
2015	Summer				1.031	25.172	0.367
	Winter		18.914	7.656			
2020	Summer				1.96	22.464	2.146
	Winter		14.569	12.001			

west direction during 2010. The situation was more acute in 2015 as most of the areas were covered by $30^{\circ}\text{C} - < 34^{\circ}\text{C}$ LST zone, expanding towards northwest, northeast and southeast directions. In 2020, a strong effect of LST was experienced with $26^{\circ}\text{C} - < 30^{\circ}\text{C}$, $30^{\circ}\text{C} - < 34^{\circ}\text{C}$ and $> 34^{\circ}\text{C}$ where the highest temperature (36.27°C) was recorded in northwest part near to city core in 2020.

The directional change of LST has a similar pattern for winter season (Fig. 8). Most directions were recorded under $< 18^{\circ}\text{C}$ LST zone with $18^{\circ}\text{C} - < 22^{\circ}\text{C}$ LST effects in several directions for 1995. In 2005, the $18^{\circ}\text{C} - < 22^{\circ}\text{C}$ LST effect was expanded to all directions from the city center. This growth pattern accelerated to 2010, when some places continued to experience $22^{\circ}\text{C} - < 26^{\circ}\text{C}$ LST effect. Between 2010 and 2015, SCC areas were dominated by $22^{\circ}\text{C} - < 26^{\circ}\text{C}$ LST effects and expanded mostly to northwest part. This trend further continued to 2020 due to excessive urban expansion in the northwest and southwest direction. The study area's thermal comfort decreases from the growth center to the outskirts, according to the seasonal LST directional variation.

Climate change, in addition to anthropogenic activities, contributes to temperature rises [80]. The glacier shrank faster, resulting global climate change, and deforestation, breaking of ice on lakes and rivers also affect the environmental viability and has exacerbated acute heat stress.

3.7. Directional change analysis of seasonal UHI distribution

Urban expansion significantly contributes the directional changes of seasonal UHI from 25 years (1995–2020). Fig. 9 illustrates the directional distribution of UHI effect from 1995 to 2030 in summer and winter seasons. In 1995, most of the directions were recorded as none UHI effects, except the vicinity of the city center which had the rest of the UHI effect. Very low and low effect was observed mostly in the northwest and northeast directions of SCC. In 2005, low, moderate and high UHI concentration was recorded near city center whereas none zone was observed outer part of the city boundary. In 2010, low and moderate effects were spread all over the directions, with high UHI impact in the growth center. Expansion of moderate zone in the center part of the city was evident for severe situation, with some very high UHI effect in the southeast direction in 2015. Between 2015 and 2020, a much stronger UHI scenario was observed in the southeast and southwest direction, covering northern part by low and very low UHI effects.

During the winter season, a similar growth trend of UHI effect was observed (Fig. 9). In 1995, most of the directions showed no UHI effect in all directions, with a very low UHI effect around the city center and northwest peripheral area. A very low UHI effect was directed to the northwest part along with proximity to city center. In 2005, growth was accelerated as the same pattern, and

in 2010, some directions were tended to experience low UHI effect in the northwest direction. The moderate UHI effect was started to observe in the east direction away from the city center, with very low effect in the northeast direction. A very low effect increase was expanded all over the city area, with moderate UHI effects expanding towards north-west and south direction between 2015 and 2020.

Reducing vegetation cover, replacement of green cover, lack of feasible planning schemes are some major reasons contributing to the increasing UHI effect in the SSC. Climate change also increases urban flooding and heat stress due to rising sea levels and extreme precipitation.

3.8. Correlation between LST and land cover indices (NDBI, NDBSI, NDVI, NDWI)

Pearson correlation analysis is a statistical method that measures the linear association between two quantitative variables [81]. It is carried out to evaluate the type and strength of the relationship between LST and other land cover indexes [82,83]. Fig. A.7 displayed a highly significant relationship between seasonal LST and all assessed land cover indexes ($p < 0.01$). In summer 1995, a strong positive association was identified between LST with NDBI and NDBSI, with an inverse correlation to NDVI and NDWI. This scenario was also experienced for both summer and winter seasons between 2010 and 2020. LST against NDVI and NDWI showed that the value of water content and green cover decreased with higher temperature differences. On the contrary, an excessive amount of bare soil and buildup growth influenced to amplify the heat over the area and increased the LST value.

Bare soil comprises the area with no vegetation cover, with lower thermal capacity to reduce temperature. In addition, bare soil and built-up areas get warmer quickly, becoming hot and colder during summer [84,85]. Impervious materials make up the road surfaces, which prevents less heat from escaping. That is why LST is much higher in rough surfaces and has less vegetation cover.

3.9. Correlation between UHI and land cover indices (NDBI, NDBSI, NDVI, NDWI)

A strong correlation was detected between the seasonal UHI effect and NDBI, NDBSI, NDVI, NDWI [86]. Higher correlation between LST and NDVI is evident that Sylhet has a lack of vegetation cover, and hence, the UHI intensity is amplified over the years (Fig. A.8). Moreover, NDBI and NDBSI are positively associated with UHI for all the years that portray the intensity of built-up growth in the study area. Again, a similar inverse severity pattern was

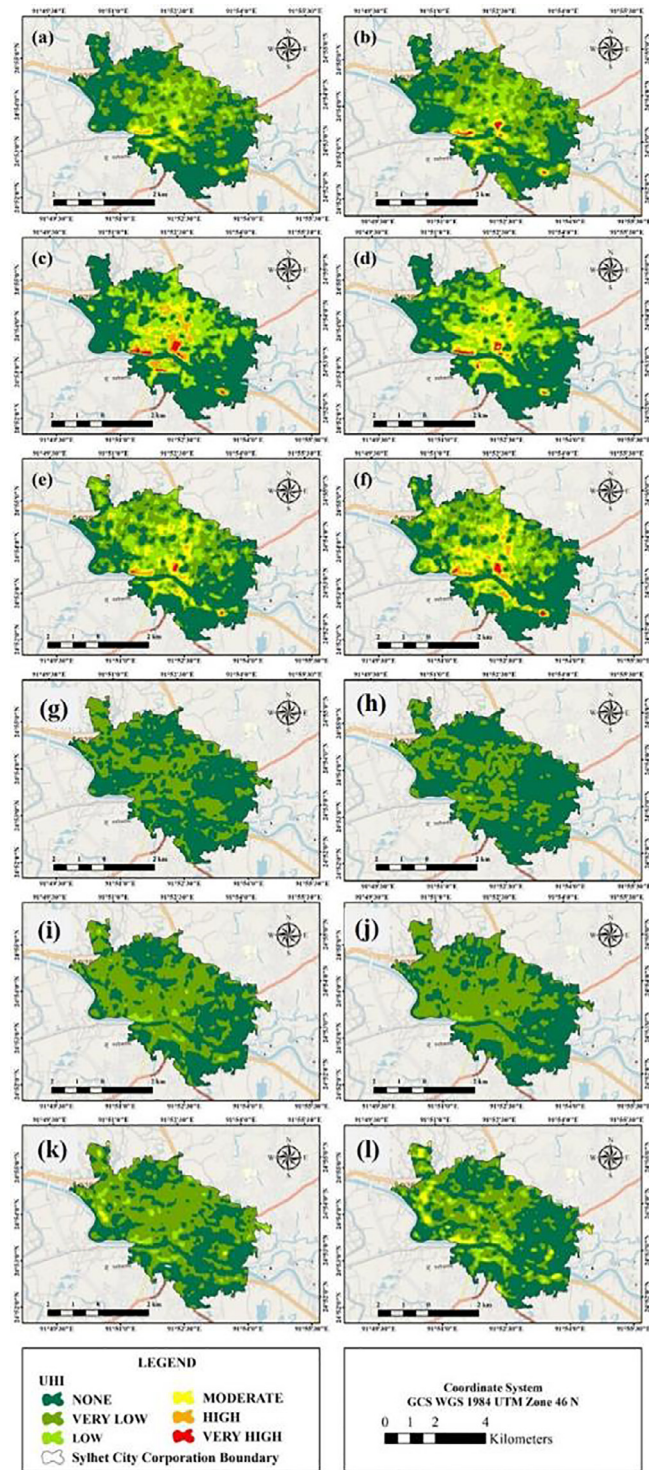


Fig. 6. Distribution of summer (a-f) and winter (g-l) UHI in the study area (a) & (g) 1995 (b) & (h) 2000 (c) & (i) 2005 (d) & (j) 2010 (e) & (k) 2015 (f) & (l) 2020.

recorded among UHI with NDVI and NDWI for both the summer and winter season.

3.9.1. Roof and pavement materials

There was a positive significance between NDBI and UHI for the study area. According to previous literature, pavement significantly contributes to increasing the UHI effect [87]. Moreover, 52.66 % built-up area was recorded in 2020 (Fig. 3), where the pavement

and roofs are covered with man-made, hard and heat absorbent surfaces [88,89]. Asphalt concrete are the most used pavement and roof surfacing material which is a prime contributor for the increasing heat effect in urban area as it can be hotter than grass surface up to 20 °C [108]. The heat capacity is in high volume on densely graded asphalt, with low albedo [90].

3.9.2. Geographic and atmospheric conditions

The regional atmospheric condition and geographic features are a powerful determinant of the heat effect and its intensity in the urban area. The day time also dramatically affect the UHI severity as pavement emissivity and radiated heat into the atmosphere increase the surface temperature during night time [91].

3.9.3. Urban sprawl and overpopulation

The density of urban area, heat absorbing impervious, and decrease of vegetation surface are the influential factors to effect UHI [92,93]. The expansion of city increase both size and breadth and the sprawling cities experience more heat waves than compact metropolitan cities [94]. Urban expansion means an increase in impervious surface and reduction of green cover, contributing severe heat island phenomenon [95]. Moreover, the gradual increase in Sylhet's population is a key driver for global warming, deforestation and biodiversity loss, which significantly contributes to UHI and energy cost acceleration.

3.9.4. Energy needs for heating and cooling

Urban growth with technological development contributes to the heat wave by increasing the amount of heating and cooling; for example, air conditioning systems used for human comfort accelerate a greater level of heat in the atmosphere [96]. Dense cities need more air conditioners for the functioning of infrastructure, which create thermal discomfort by increasing the heat of the city in the summer season[109]. But the UHI effect can be used in winter by reducing the electricity demand for room heaters. The storage of summer heat for winter use cuts the bills and boosts the renewables by heat pump [97].

3.10. Correlation between UHI and digital elevation model (DEM)

The relationship between the heat effect and elevation of the study area illustrated in Fig. A9 achieved by retrieving ASTER data from USGS at 30 m resolution. The lowest and highest elevation is found undulated out as –11 m and 56 m, respectively. The comparison between the UHI effect and DEM model in the summer and winter season have been shown in the scatter plot (Fig. A9 a & b). Comparatively better correlation was recorded for the summer season unlike winter season. Moreover, highest association was observed from 2010 to 2020, where the trend was remaining same for the winter season over the years.

The effects of LST phenomenon over land surface increase the amount of heat effect in particular area [72]. Moreover, the association between LST and topographic characteristics have high significance which can be differed over time depending on the amount of received solar energy[98]. Sada Pathor in Volaganj, Chandmari Tila, Bichanakandi in Gowainghat are the highly elevated area of Sylhet district. Low correlation during the winter season was observed due to highly elevated hilly area in the northeastern and north western direction beside those high altitude area. In addition, the emissivity is maximum in the rocky texture of hilly area than vegetation cover[99]. Therefore. The raising trend of UHI was noticed in the summer season than winter as a result of less green cover in the high elevated zones. However, UHI has influenced by factors like surface roughness, extent of green cover etc. [100]. Hence, these local parameters effect the high UHI value along with elevation.

Table 4Area (Km^2) wise UHI distribution.

Year	Season	Values of UHI					
		< 0	0 – 0.75	0.75 – 1.5	1.5 – 2.25	2.25 – 3	> 3
		None	Very Low	Low	Moderate	High	Very High
1995	Summer	11.876	9.527	4.193	0.716	0.258	
	Winter	17.111	9.459				
2000	Summer	14.07	8.469	3.244	0.712	0.062	0.013
	Winter	17.616	8.86	0.094			
2005	Summer	15.45	3.009	5.267	1.545	1.021	0.278
	Winter	11.66	13.481	1.429			
2010	Summer	13.749	2.953	5.658	2.23	1.508	0.472
	Winter	9.991	11.817	4.762			
2015	Summer	10.89	6.327	4.94	1.728	2.035	0.65
	Winter	12.291	12.642	0.704	0.933		
2020	Summer	11.311	5.764	3.709	1.51	2.65	1.626
	Winter	10.203	13.04	1.829	1.498		

Table 5

Correlations between built-up area and summer mean LST and UHI from 1995 to 2020.

		Built up area (km^2)	Mean LST summer ($^{\circ}\text{C}$)	Mean UHI summer
Built up area (km^2)	Pearson	1	0.910*	0.982**
	CorrelationSig (2 – tailed)	6	0.012	0.003
Mean LST Summer ($^{\circ}\text{C}$)	N		6	6
	Pearson	0.910*	1	0.942**
Mean UHI summer	CorrelationSig (2 – tailed)	0.012	0.005	0.005
	N	6	6	6
Mean UHI summer	Pearson	0.982**	0.942**	1
	CorrelationSig (2 – tailed)	0.002	0.005	0.005
N				

*Correlation is significant at the 0.05 level (2-tailed).

**. Correlation is significant at the 0.01 level (2-tailed).

Table 6

Correlations between built-up area and winter mean LST and UHI from 1995 to 2020.

		Built up area (km^2)	Mean LST winter ($^{\circ}\text{C}$)	Mean UHI winter
Built up area (km^2)	Pearson	1	0.964**	0.911*
	CorrelationSig (2 – tailed)	6	0.002	0.005
Mean LST Winter ($^{\circ}\text{C}$)	N		6	6
	Pearson	0.964**	1	0.862*
Mean UHI winter	CorrelationSig (2 – tailed)	0.002	0.027	0.027
	N	6	6	6
Mean UHI winter	Pearson	0.911*	0.862*	1
	CorrelationSig (2 – tailed)	0.011	0.027	0.027
N				

**. Correlation is significant at the 0.01 level (2-tailed).

*. Correlation is significant at the 0.05 level (2-tailed).

3.11. Correlation between built-up area and mean value of LST and UHI

The association of built-up up area with seasonal LST and UHI is found significant ($P < 0.01$). With LST and UHI, the correlation pattern was positive, where the most significant one is the mean UHI and Built-up area ($r = 0.982$) in the summer season (Table 5). In

contrast, the strongest association was found between built-up area and LST for winter ($r = 0.964$). Therefore, a positive relationship was prominent between mean LST and mean UHI were 0.942 ($p < 0.01$) and 0.862 ($p < 0.05$), respectively (Table 6).

Building dominated urban areas, producing strong heat radiation, which increases the LST [102]. In addition, the continuous increase in LST results in a gradual increase of UHI [103]. Increased

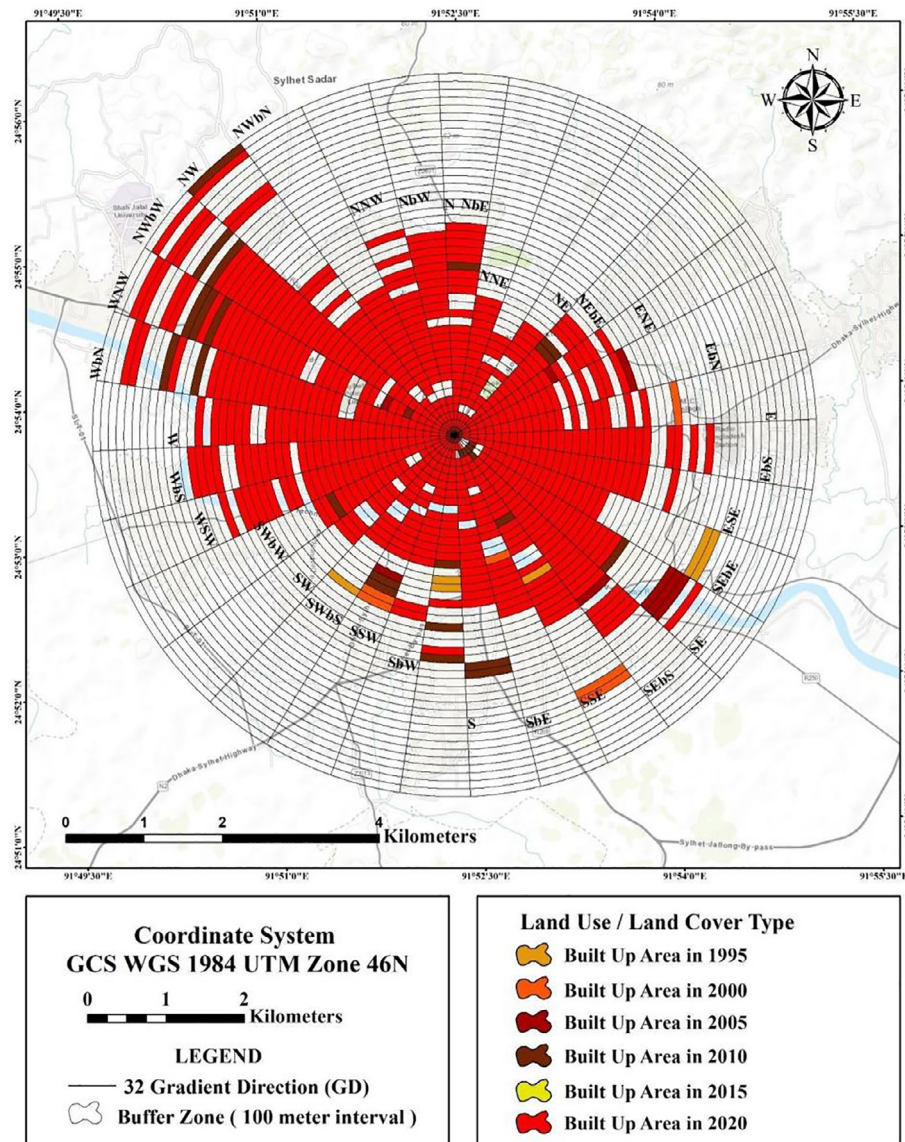


Fig. 7. Directional Change of built-up areas from 1995 to 2020.

peak energy consumption, greenhouse emission, air pollution and excessive heat-related diseases will impact communities due to increased UHI [104,105].

3.12. LST variation over different land cover classes

The zonal statistics algorithm was applied to measure the mean LST distribution over selected LULC categories. The distribution pattern of mean LST was recorded under various land cover classes (Fig. A.10), for both seasons. In the 1995 to 2020 summer season, mean LST's impacts were exacerbated mostly in built-up areas and bare land at 9.3 °C and 6.64 °C, respectively. Water bodies had the lowest mean LST, which increased gradually with the rate of 0.21 °C in 25 years. Likewise, the mean LST changing pattern was noticed in vegetation land cover between 2015 and 2020 at 2.53 °C.

During winter, minimal mean LST fluctuation was experienced for all land cover classes. In 2005 to 2015, the mean LST of bare and built-up areas was relatively stable at 22.64 °C and 23.08 °C, respectively, with a slight increase in 2020. In addition, vegetation

and water body were observed static at 21.22 °C, and 20.05 °C, respectively for 2000, 2005, 2015 and 2020.

Fig. 10 demonstrated the seasonal LST distribution pattern for four LULC categories for 1995 to 2020. During the summer, highest LST ranges were seen in built-up areas from 22 °C - < 26 °C (10.46 %) in 1995, 22 °C - < 26 °C (12.33 %) and 26 °C - < 30 °C (10.67 %) in 2000, 26 °C - < 30 °C (26.43 %) in 2005, 26 °C - < 30 °C (36.71 %) in 2010, 30 °C - < 34 °C (48.51 %) in 2015, 30 °C - < 34 °C (44.92 %) and > 34 °C (7.22 %) in 2020 (Figure 23). Bare land also showed high LST from 26 °C - < 30 °C (12.48 %) to 30 °C - < 34 °C (5.03 %) in 1995 to 2015, respectively. Between 1995 and 2020, 36.52 % LST of vegetation cover was recorded to increase in the range of 30 °C - < 34 °C. In water bodies, the lowest temperature was observed in 1995 (19.34 °C) and 2020 (32.71 °C), whereas the highest 34.13 °C temperature was reflected from vegetation cover in 2020.

During the winter of 2020, LST in the range of (22 °C - < 26 °C) was recorded in 25.87 % for urban area and 17 % for vegetation cover. Moreover, no LULC categories was found in 26 °C - < 30 °C, 30 °C - < 34 °C and > 34 °C LST zones. In 2020, the lowest

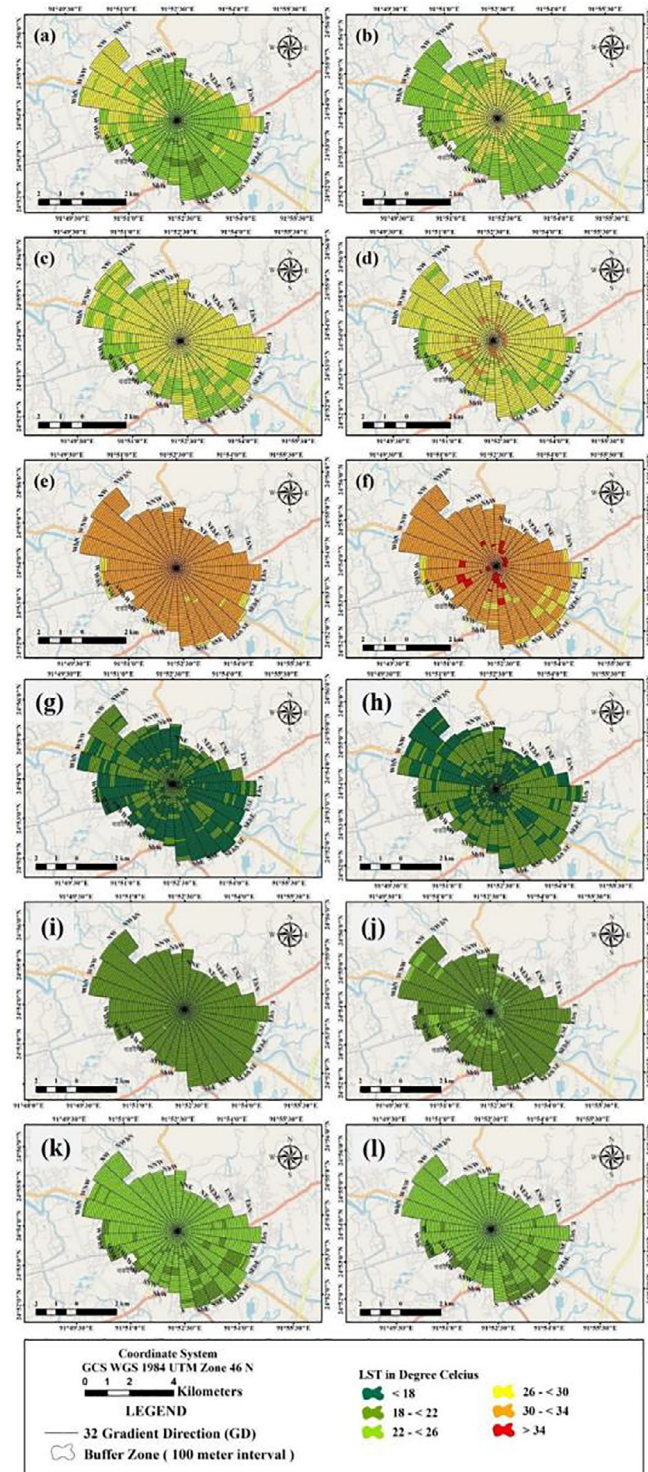


Fig. 8. Directional change of summer (a-f) and winter (g-l) LST in the study area (a) & (g) 1995 (b) & (h) 2000 (c) & (i) 2005 (d) & (j) 2010 (e) & (k) 2015 (f) & (l) 2020.

temperatures were 19.44 % and 21.82 % for water body and bare land, respectively, whereas the highest temperatures for urban areas were 36.27 °C.

The seasonal LST of different land cover classes indicated that the water body was under the least temperature zone as it has the ability of less transpiration and heat absorption tendency from 1995 to 2020. Due to massive sunlight reflection and impervious surface, a high temperature was recorded for the built-up area. Urban infrastructure produces long thermal infrared waves that

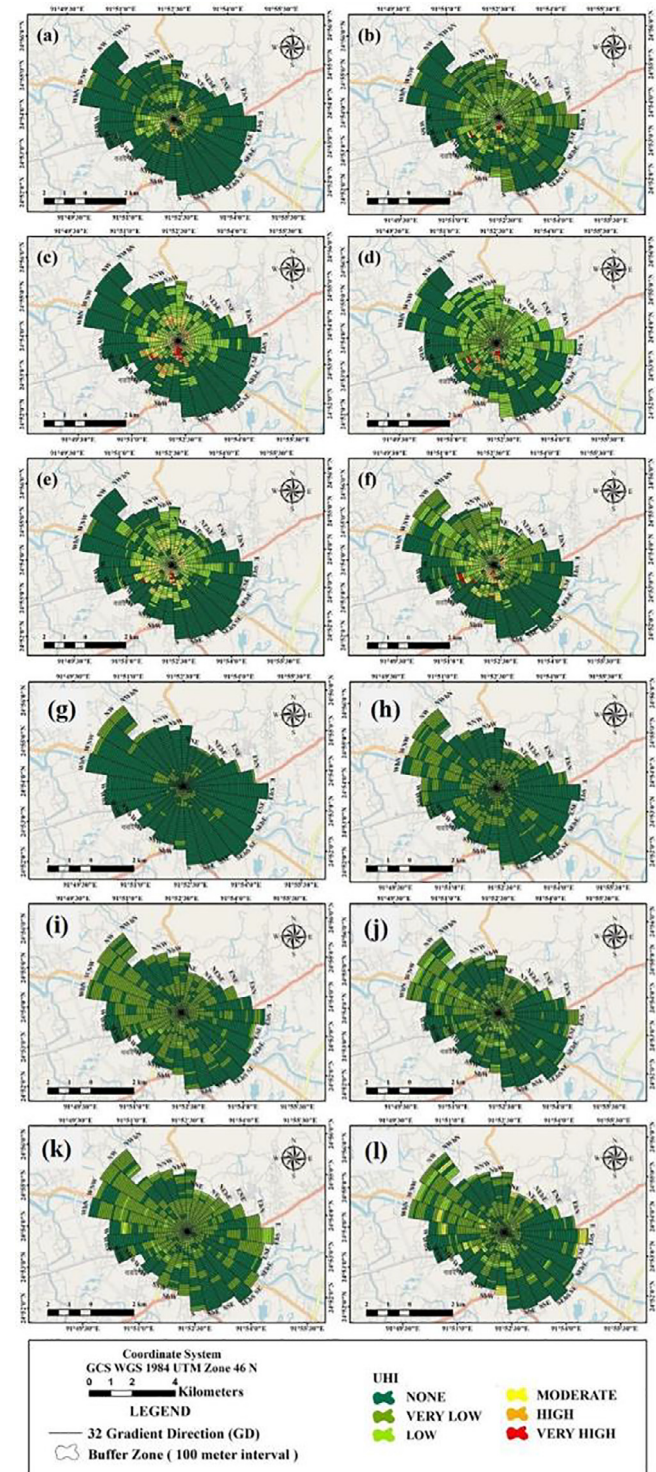


Fig. 9. Directional Change of summer (a-f) and winter (g-l) UHI in the study area (a) & (g) 1995 (b) & (h) 2000 (c) & (i) 2005 (d) & (j) 2010 (e) & (k) 2015 (f) & (l) 2020.

increase surface temperature [101]. This gradual increment of LST is the reason for the intensified effect of UHI in urban areas.

3.13. UHI distribution over different land cover classes

Seasonal UHI (summer and winter) distribution over different LULC is illustrated for 1995, 2000, 2005, 2010, 2015 and 2020 in Fig. 11. In summer, a very high UHI effect was noticed for

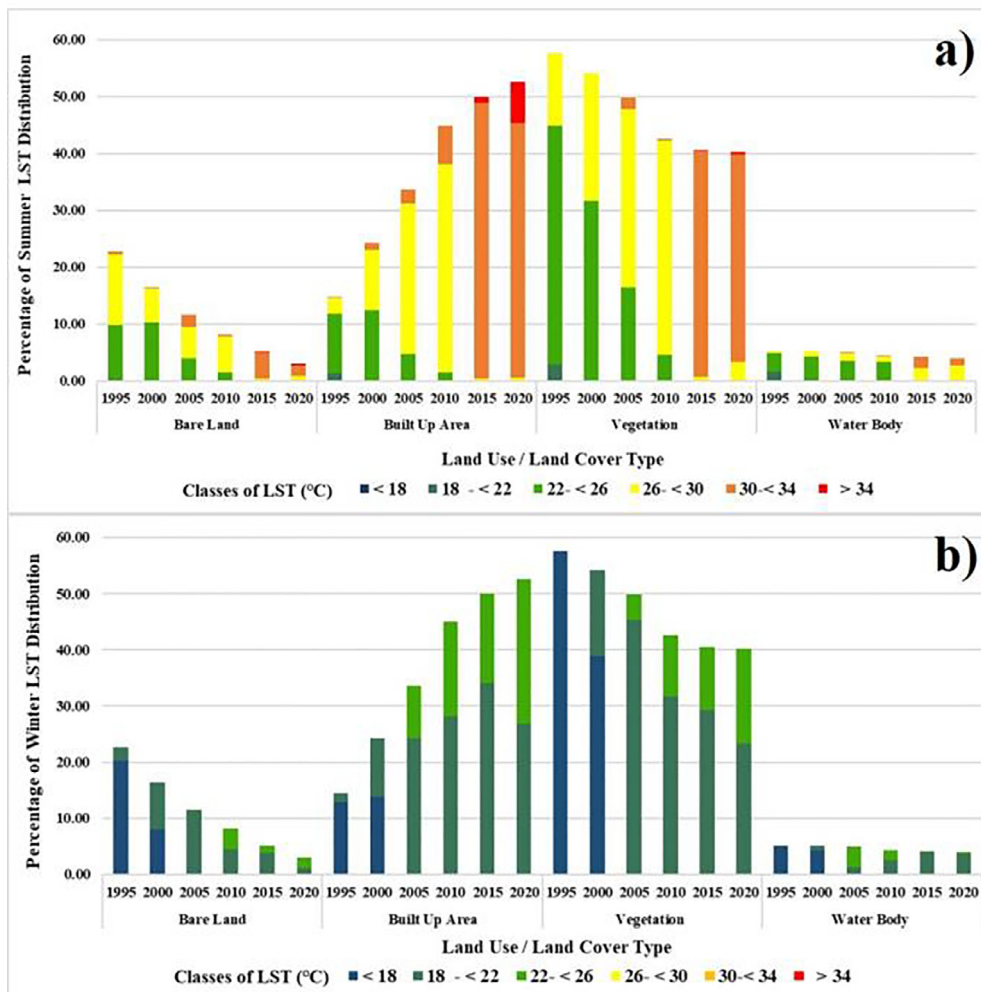


Fig. 10. (a) Summer and (b) Winter LST distribution over different land cover classes from 1995 to 2020.

built-up areas where water bodies and bare land were found to moderate UHI impact (Fig. 11). The exceptional impact was recorded for vegetation in 2020, where it was experienced a high and very high UHI effect, followed by 2.56 % and 3.33 %, respectively. Very high UHI zone was increased from 1.90 % to 2.51 % during 2015 to 2020. Bare land had a very lower UHI effect, which increased by 0.28 % in 2020.

In the winter season, similar UHI effects were found in urban areas and vegetation cover was similar to the summer season. During 1995, 12.45 %, 8.32 % and 42.78 % none UHI effects were experienced by bare land, built-up area and vegetation. In 2015 and 2020, 3.45 % and 5.67 % moderate UHI were recorded in built-up areas where high and very high zones were not found in any LULC classes.

UHI effect is significantly related to LST, that's why it is most prominent in buildings and pavements. These building materials absorb more heat than water bodies and green covers. Introducing renewable energies rather than fossil fuels, increasing open and green space, incorporating reflective infrastructure materials, and integrating sustainable water management in urban planning will effectively minimize the effect of UHI in the study area.

3.14. Future urban expansion scenario

3.14.1. Model validation

The model was validated for 2015 and 2020 year by using reference and predicted built-up area data. A detailed Kappa and

ROC curve illustrated the model performance. Kappa parameters compared the actual and predicted built-up area of 2015 and 2020, with 98.66 % and 97.45 % kappa overall value (Table 7). Besides that, ROC showed referenced line that must fit within AUC curve to estimate the usefulness of the model as 0.898 and 0.917 for 2015 and 2020, respectively (Fig. 12). That AUC value portrayed that the model had 89.9 % and 91.7 % power to identify the built-up classes correctly. Both values were significantly higher and performed excellently.

3.14.2. Predicting future urban expansion and land conversion

Fig. 13 represents the predicted built-up area for 2025 and 2030 using MOLUSCE Plugin in Q-GIS interface. 56.62 % and 58.93 % built-up area were observed in SCC area for 2015 and 2030, respectively, with the rate of 0.08 km² built-up growth per year.

Simulated land cover conversion to the built-up area was measured for a different time frame in Fig. 14. Conversion from vegetation to built-up area was expected as 32.04 % and 34.78 % for 1995 to 2025 and 1995 to 2030, respectively, with 11.92 % and 11.98 % conversion for bare land to built-up area (Fig. 15). Waterbody was observed as less converted LULC class among four at a 1.46 % conversion rate between 1995 and 2030.

New educational institutions were established to improve the quality of research as well as develop and extend existing facilities. This existing and proposed infrastructure influences further urban expansion by converting natural land use. Sheikh Russell Textile Engineering College, Sylhet Textile Institution, Sylhet Marine

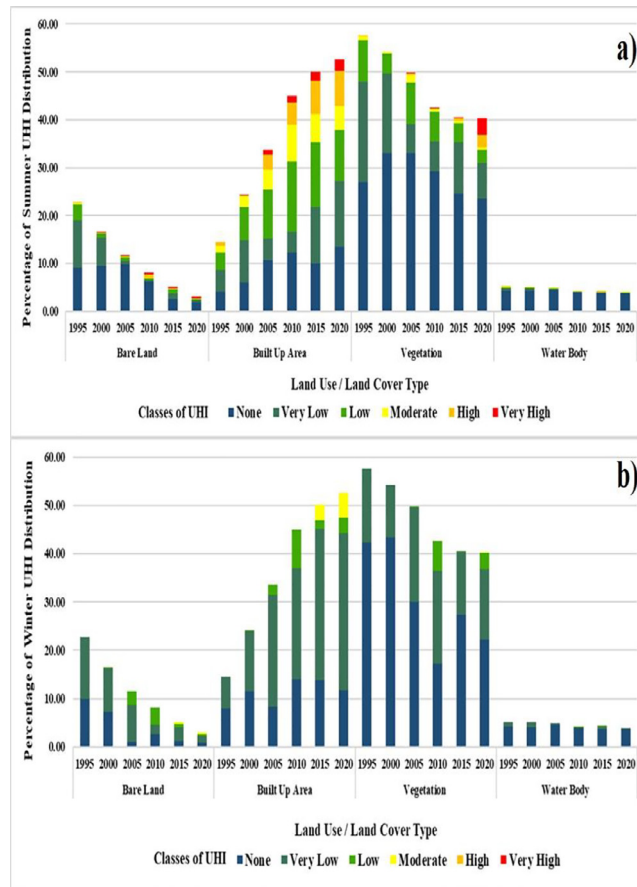


Fig. 11. (a) Summer and (b) Winter UHI distribution over different land cover classes from 1995 to 2020.

Academy are the institutions which influence excessive built-up growth surrounding those institutions in the city core.

3.15. Predicted scenario of future seasonal LST

The seasonal UHI change analysis observed tremendous surface temperature changes from 1995 to 2020. An ANN model was conducted to simulate future surface temperature distribution. Kappa values validated the accuracy of the model by using actual and predicted seasonal LST for 2015 and 2020. Overall, Kappa was $> 95\%$ for both summer and winter LST values, indicating strong accuracy of predicted LST (Table 8). Therefore, the prediction of future LST distribution is important over the study area.

LST maps and variations were predicted for summer and winter 2025 and 2030 in Fig. 16. According to prior LST distribution, a subsequent increase in LST was recorded for 2025 and 2030. During summer, no area will be affected in temperatures below 26°C in 2025 and 2030. The result also shows that 14.84 km^2 area will fall under $30^{\circ}\text{C} - < 34^{\circ}\text{C}$ temperature in 2025, which will increase to

14.95 km^2 in 2030 (Table 9). Compare to 2020, area will be expected to extend from 2.14 km^2 in 2020 to 11.23 km^2 in 2030 in the highest LST zone ($> 34^{\circ}\text{C}$) in total 9.08 km^2 (Fig. 17). Between 1995 and 2030, $30^{\circ}\text{C} - < 34^{\circ}\text{C}$ LST zone will be increased by 3.94 km^2 area. On the contrary, $22^{\circ}\text{C} - < 26^{\circ}\text{C}$ and $26^{\circ}\text{C} - < 30^{\circ}\text{C}$ LST zones will be decreased as 17.37 km^2 and 6.19 km^2 , respectively. During the summer season, a steep angle of sun touches the ground causing an increase in temperature gradually with an increase in the built-up area.

The winter LST distribution was predicted for 2025 and 2030 (Fig. 16). There is no possibility to increase the temperature under $> 34^{\circ}\text{C}$ zone, with a significant rise of $22^{\circ}\text{C} - 26^{\circ}\text{C}$ LST zone as 25.29 km^2 and 13.29 km^2 between 1995 and 2030 and 2020–2030, respectively (Fig. 17).

According to a prior study, several explanatory factors such as rapid urbanization and large-scale declination of vegetation land intensify the thermal effect of the city area [11,28]. The dominance of built-up area and reduction of water bodies and green spaces will significantly increase the high LST area. In addition, Global warming, changes in surface characteristics, greenhouse effect are vital reasons even if fast urbanization is taking place. Predicted LST for the study area demonstrates how the temperature will rise, resulting in a higher UHI effect.

3.16. Predicted scenario of future seasonal UHI distribution

The increasing trends of the UHI effect over the study area necessitate the simulation of future seasonal UHI patterns (Fig. 18). The neural network approach was adopted to predict the seasonal distribution of UHI for 2015 and 2020. Overall, Kappa values showed excellent accuracy for 2015 and 2020 UHI distribution as 0.95 and 0.97 for summer and winter 2015 and 0.96 and 0.95 for summer and winter 2020, indicating strong accuracy (Table 10).

Fig. 18 shows the UHI distribution pattern for 2025 and 2030 where a moderate UHI effect was observed prominently in 12.56 km^2 area for 2025. Besides that, in future, no area was comprised of none UHI effect (Table 11). Between 2020 and 2030, very high UHI effect will certainly be enhanced by 0.39 km^2 and none and very low effect will be reduced by 11.31 km^2 and 5.74 km^2 area, respectively (Fig. 19 and Table 11).

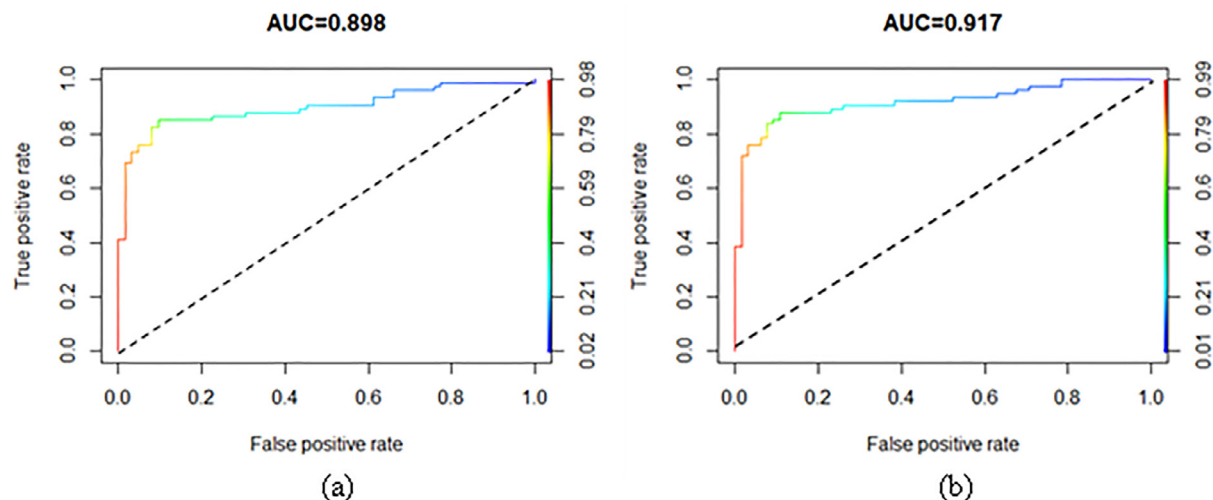
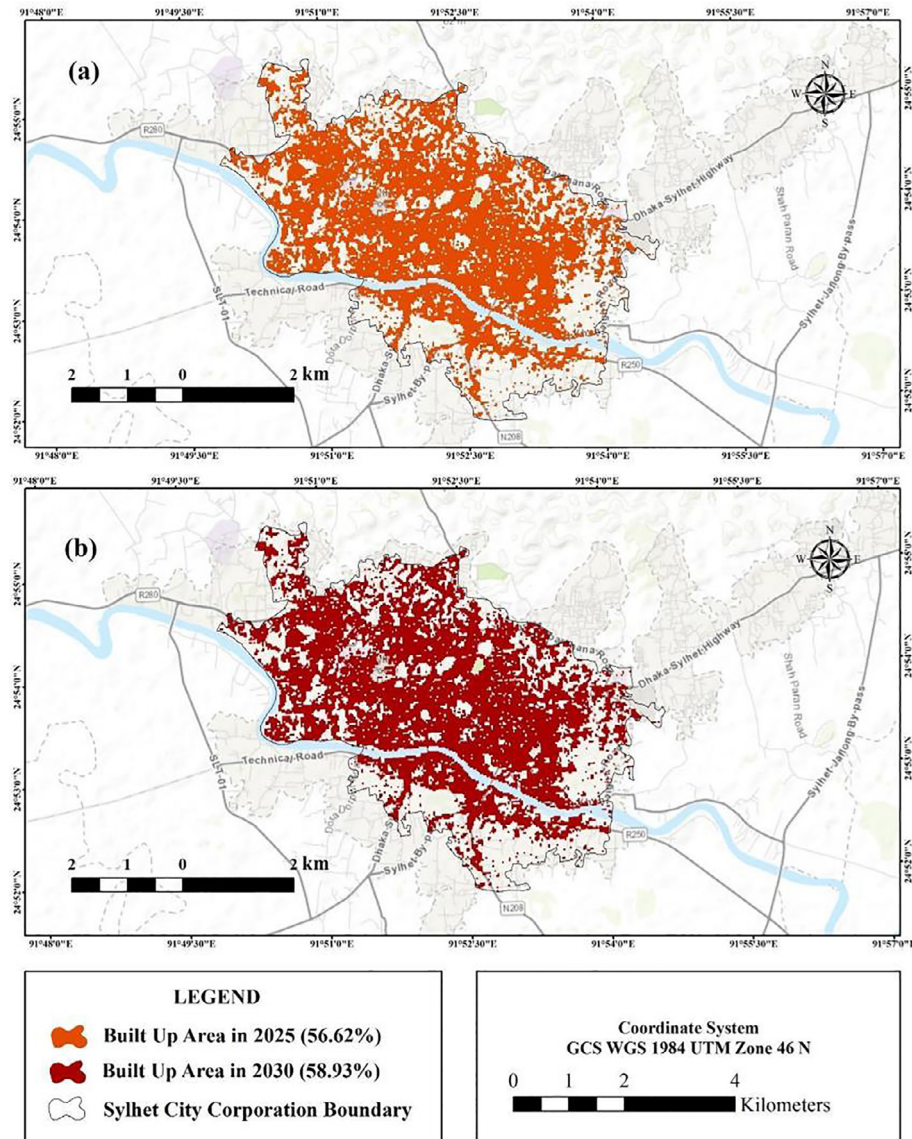
The predicted winter UHI was observed in Fig. 18 where half of the study area (14.70 km^2) will experience (1.5 – 2.25) moderate UHI effect by 2030. Very low and low effects will be reduced as 17.11 km^2 and 8.75 km^2 area, respectively, in the 30 years (1995–2025). Only 0.25 km^2 will likely be recorded under the high UHI zone (Fig. 19 and Table 11).

High UHI will likely to concentrate in the city core, whereas the periphery area will experience low UHI effect in Fig. 18. The manufacturing, metal industries, chemical and polymer industries are haphazardly growing in the CBD, therefore UHI effect is intensified in the city core. Excessive energy demand, accelerated greenhouse emissions and degraded air quality will amplify the seasonal UHI effect and posing a threat to natural water environments (rivers, ponds, oceans etc.) and urban health. Moreover, development extends from city core to the periphery of SCC, as industries (e.g.,

Table 7

ANN model validation for predicted built-up areas.

Kappa parameter for model validation in Q-GIS MOLUSCE Plugin Module				
Year	% Of Correctness	Kappa (histo)	Kappa (loc)	Kappa (Overall)
2015	96.8243	0.9648	0.9866	0.9485
2020	95.3784	0.9572	0.9745	0.9658

**Fig. 12.** ROC curve for LULC classes (a) 2015 (b) 2020.**Fig. 13.** Predicted built-up area for (a) 2025 and (b) 2030.

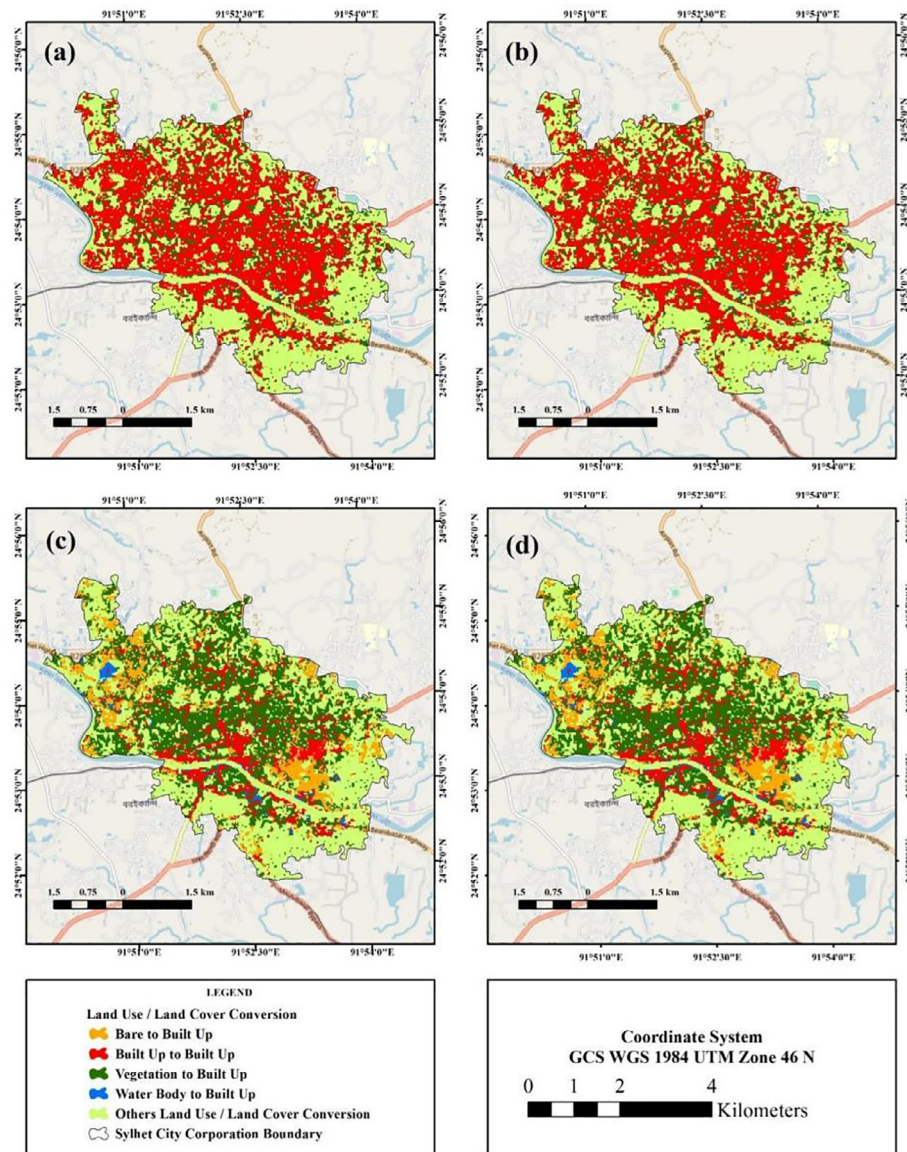


Fig. 14. Conversion from different land cover classes to built-up area (predicted) for (a) 2020–2025, (b) 2020–2030, (c) 1995–2025, (d) 1995–2030.

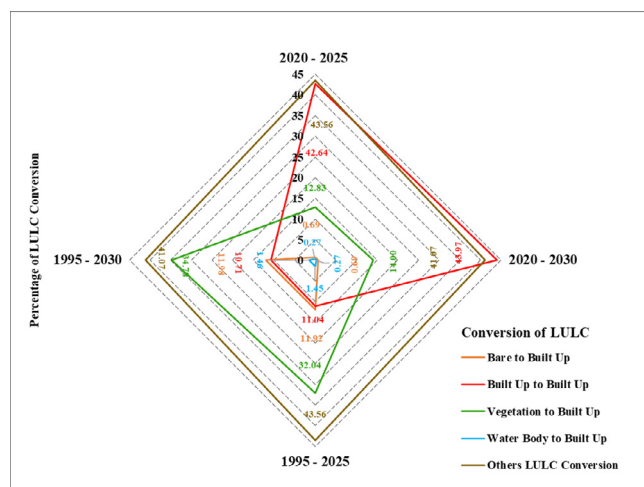


Fig. 15. Spider diagram showing percentage of conversion from different land cover classes to built-up area in 2020–2025, 2020–2030, 1995–2025, 1995–2030.

Table 8
ANN model validation for predicted seasonal LST.

Kappa parameter for model validation in Q-GIS MOLUSCE Plugin Module

Year	Season	% Of Correctness	Kappa (histo)	Kappa (loc)	Kappa (Overall)
2015	Summer	98.6172	0.9094	0.9475	0.97708
2015	Winter	99.0822	0.9235	0.9785	0.9532
2020	Summer	92.5326	0.9369	0.9988	0.9684
2020	Winter	95.9854	0.9281	0.9654	0.9823

Steel, manufacturing, polymer etc.) tend to establish near Surma River and alter the vegetation cover into an impervious surface. To offset the UHI effect, planned development is needed in the rural area without destroying the existing urban infrastructure. The implication of green belt policy can be a solution to protect country areas by restricting urban sprawl. Light-colored building materials, green cover, tree plantations, white roof, and renewable energy can reduce the UHI effect [106,107].

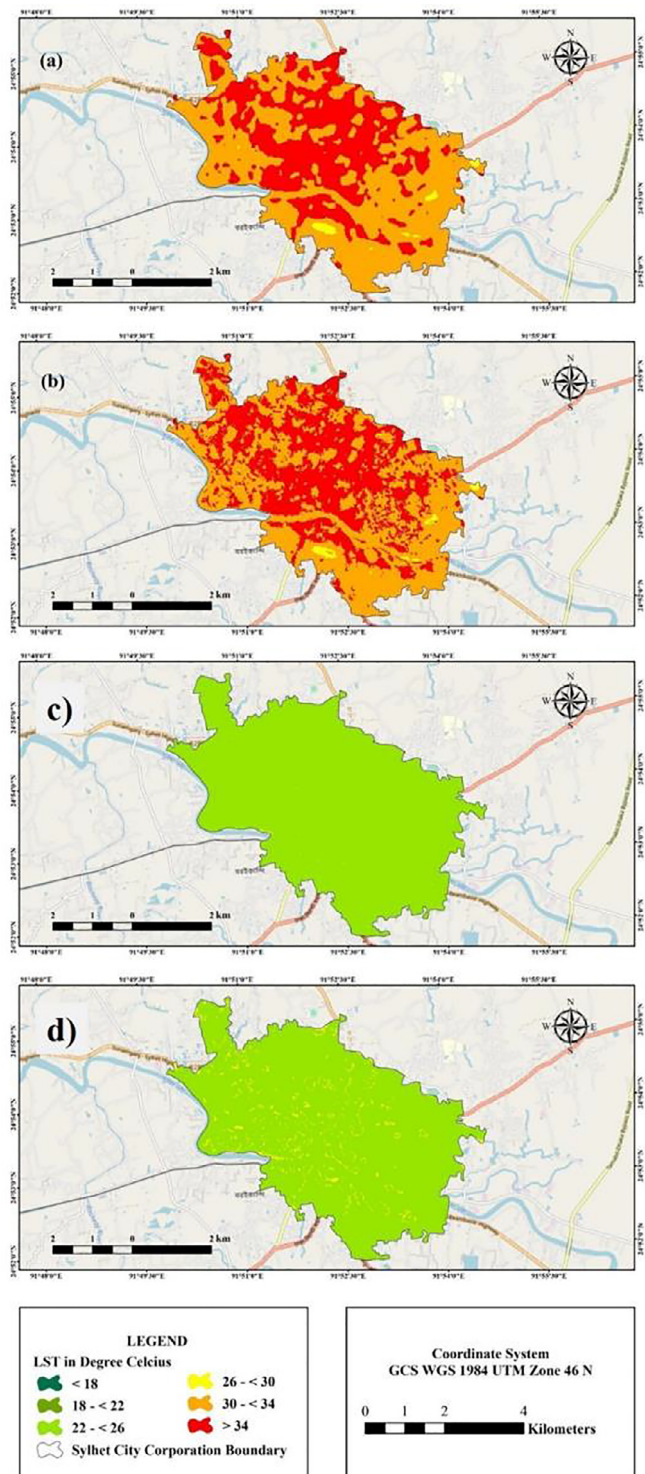


Fig. 16. Predicted summer (a&b) and winter (c&d) LST distribution for (a) & (c) 2025 and (b) & (d) 2030.

Table 9
Area wise predicted seasonal LST distribution.

Year	Season	LST Range in °C Area (Km ²)					
		< 18	18 - < 22	22 - < 26	26 - < 30	30 - < 34	> 34
2025	Summer				1.282	14.848	10.440
	Winter			26.255	0.315	0.393	14.950
2030	Summer				25.29	1.28	11.227
	Winter						

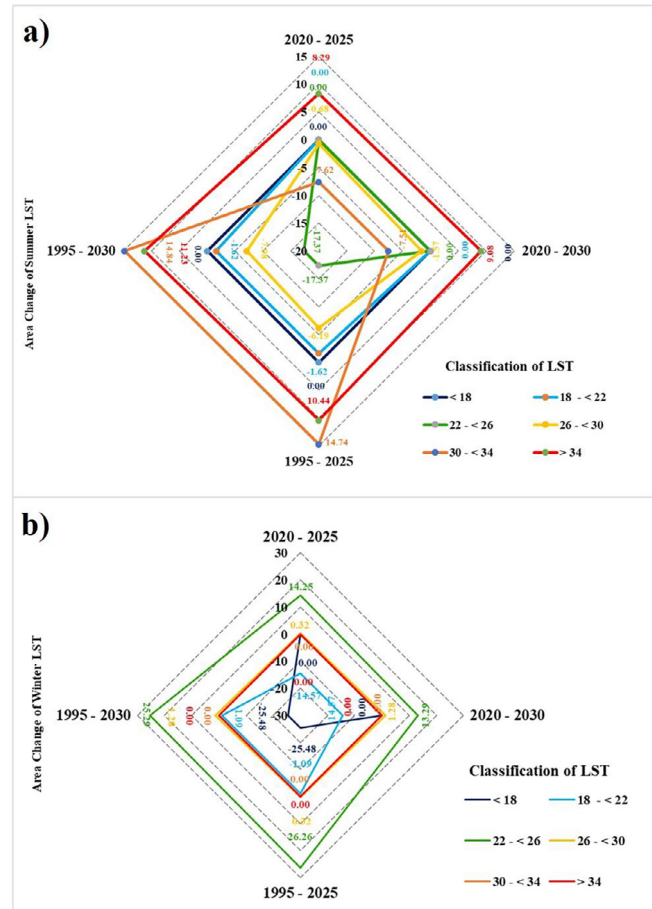


Fig. 17. Spider diagram showing area changes for (a) summer and (b) winter LST in 2020-2025, 2020-2030, 1995-2025 and 1995-2030.

4. Conclusion and avenue for future research

LULC dynamics and the resulting environmental changes are considered one of the most critical challenges towards achieving environmental sustainability in both developed and developing countries. Rapid urbanization due to population growth and declination in vegetative areas contributes to environmental degradation and accelerates the thermal environment. Due to the increase in future uncertainty caused by rapid LULC changes and environmental degradation, assessment and prediction of spatiotemporal LULC consequences have become increasingly important in sustainable environmental planning and management. Using the integrated GIS and RS technologies with machine learning algorithms in the Sylhet City of Bangladesh, this study investigated and predicted the LULC and seasonal UHI effects from 1995 to 2030, having been the first time through Landsat imageries. This study also identified the directional UHI variations and assessed the responses of seasonal UHI variations to different land use indices.

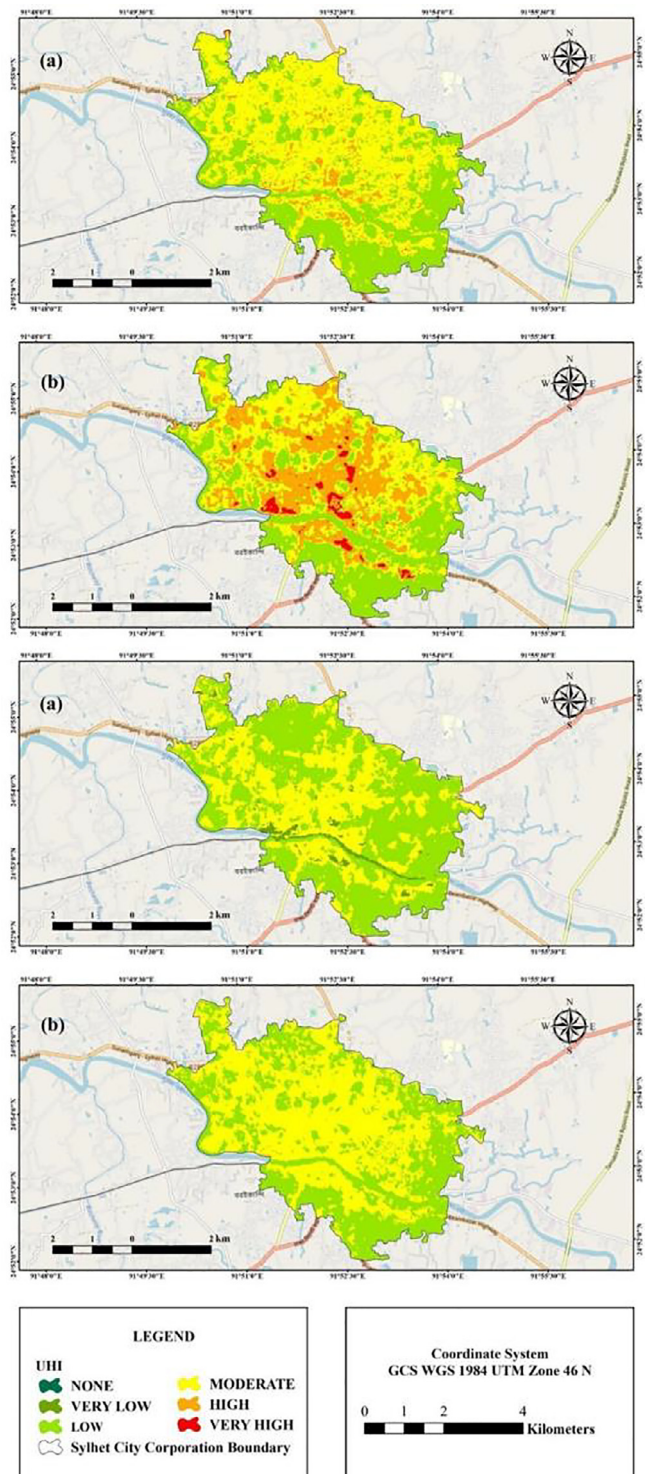


Fig. 18. Predicted summer (a&b) and winter (c&d) UHI distribution for (a) & (c) 2025 and (b) & (d) 2030.

Table 10
ANN model validation for predicted seasonal UHI.

Kappa parameter for model validation in Q-GIS MOLUSCE Plugin Module					
Year	Season	% Of Correctness	Kappa (histo)	Kappa (loc)	Kappa (Overall)
2015	Summer	90.2035	0.9486	0.9685	0.9567
2015	Winter	95.9649	0.9273	0.9828	0.9734
2020	Summer	95.8153	0.9778	0.9439	0.9655
2020	Winter	92.2516	0.9058	0.9626	0.9526

Table 11
Area wise predicted seasonal UHI distribution.

Year	Season	Area (Km ²)UHI (Value)					
		< 0	0 – 0.75	0.75 – 1.5	1.5 – 2.25	2.25 – 3	> 3
		None	Very Low	Low	Moderate	High	Very High
2025	Summer	8.782	12.560	3.302	1.926		
	Winter	0.703	15.489	10.378			
2030	Summer	8.396	9.090	7.069	2.015		
	Winter	11.620	14.700	0.250			

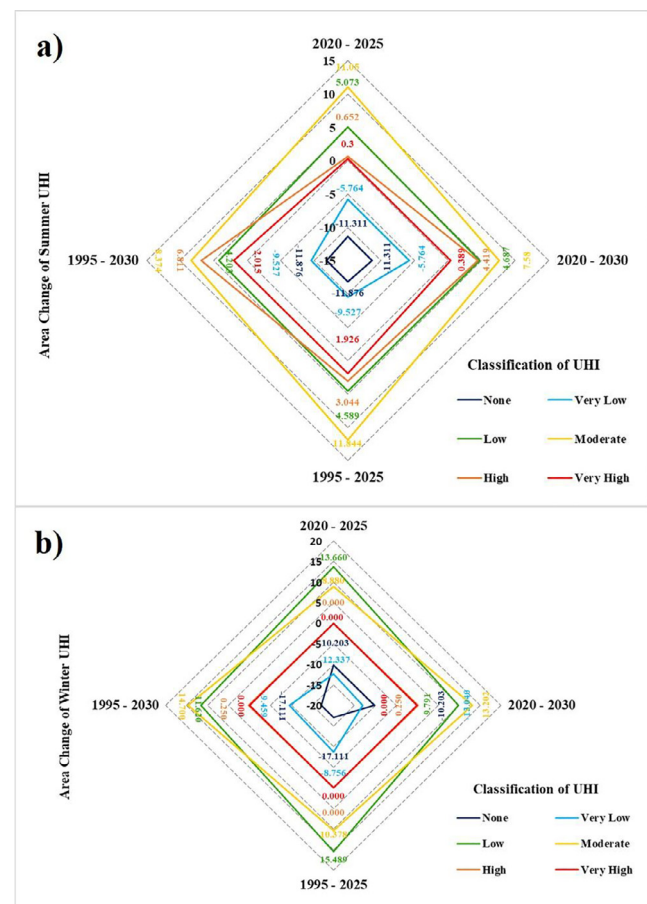


Fig. 19. Spider diagram showing area changes for (a) summer and (b) winter UHI in 2020–2025, 2020–2030, 1995–2025 and 1995–2030.

Finding shows that rapid urbanization increased built-up areas in Sylhet City by more than three times (14.52 % to 50.06 %) from 1995 to 2020. About 29.45 % of vegetation cover has been transformed into built-up cover. This abrupt LULC change increased the seasonal LST and contributed to the study area's large spatial variations in UHI patterns. From 1995 to 2020, areas with moder-

ate UHI increased from 3 % to 6 %, areas with high UHI from 1 % to 10 %, and areas with very high UHI from 0 % to 6 % in summer. The winter season UHI variations show that areas with none UHI decreased from 64 % to 38 %, and areas with low and moderate UHI increased from 0 % to 7 % and 6 %, respectively. However, the correlation between UHI and land use indices shows strong variation with higher R^2 values in Sylhet City, which implies that rapid LULC changes strongly influence the UHI. The correlation analysis value of 0.982 between built-up area expansion and summer season UHI dynamics and 0.911 for winter indicates that the UHI is significantly affected by built-up expansion at 0.01 and 0.05 significant levels, respectively.

The relationship between UHI and land use indices found in this research gives a practical statistical approach to quantify the impacts of different LULC dynamics on UHI at a local and national scale. Using this relationship, this study forecasted UHI caused by LULC change in the future by integrating the LULC, LST, and LULC indices through machine learning algorithms. The simulated future LULC shows that about 34.78 % of vegetation cover will be transformed into built-up cover during the study period. The prediction of LST for 2030 shows that, about 42 % of area's LST will be above 34 °C in summer and 95 % of areas LST will range between 22 °C – 26 °C in winter due to the increase of built-up areas and degradation of vegetative areas in the future. As a result, the High and Very High UHI-affected area percentages will increase to 25.63 % and 7.58 %, respectively, in the summer 2030. In winter 2030, about 55.33 % of areas will face moderate UHI effects and 1 % will face High UHI effects, whereas, in winter 1995, all the areas were under the None (64.40 %) and Very Low (35.60 %) UHI category.

Though climate change has also significantly influenced UHI variations, this study did not consider the meteorological variables to predict future UHI patterns. Therefore, the priority of integrating meteorological and hydrological factors and the consequences of environmental changes on UHI should be the future study. It is also necessary to investigate the contribution of daily human activities to the urban thermal environment to better understand the impacts of urban form on UHI in more detail. The overall study will help planners, researchers, and policymakers better understand and use the urban landscape sustainably, considering the future potential aspects.

CRediT authorship contribution statement

Milan Saha: Visualization, Validation, Supervision, Resources, Project administration, Funding acquisition, Conceptualization.

Abdulla Al Kafy: Writing – review & editing, Writing – original draft, Validation, Supervision, Resources, Methodology, Investigation, Formal analysis, Data curation, Conceptualization, Project administration. **Arpita Bakshi:** Visualization, Validation, Software, Resources, Methodology, Formal analysis, Data curation, Writing – review & editing. **Abdullah-Al-Faisal:** Writing – review & editing, Writing – original draft, Validation, Supervision, Resources, Methodology, Investigation, Formal analysis, Project administration. **Abdulaziz I. Almulhim:** Investigation, Supervision, Validation, Visualization, Writing – review & editing. **Zullyadini A. Rahaman:** Investigation, Supervision, Validation, Visualization, Writing – review & editing. **Abdullah Al Rakib:** Writing – review & editing, Writing – original draft, Visualization, Resources. **Md. Abdul Fattah:** Writing – review & editing, Writing – original draft, Validation, Supervision, Investigation, Conceptualization. **Kaniz Shaleha Akter:** Writing – original draft, Methodology, Validation, Visualization, Writing – review & editing. **Muhammad Tauhidur Rahman:** Writing – review & editing, Writing – original draft, Validation, Supervision, Investigation, Conceptualization. **Maomao Zhang:** Writing – original draft, Validation, Supervision, Project administration, Data curation. **R. Rathi:** Writing – original draft, Validation, Supervision, Project administration, Data curation.

Data availability

Data will be made available on request.

Declaration of Competing Interest

The authors declare that they have no known competing financial interests or personal relationships that could have appeared to influence the work reported in this paper.

Acknowledgements

The authors would like to thank the US Geological Survey for assisting this research with datasets. The authors would also like to thank the Dynamic Institute of Geospatial Observation Network – DIGON (<http://digonresearch.org/>) research and consultancy firm experts for proofreading the manuscript and providing technical support in this research.

Data availability

Data will be made available on request.

Appendix

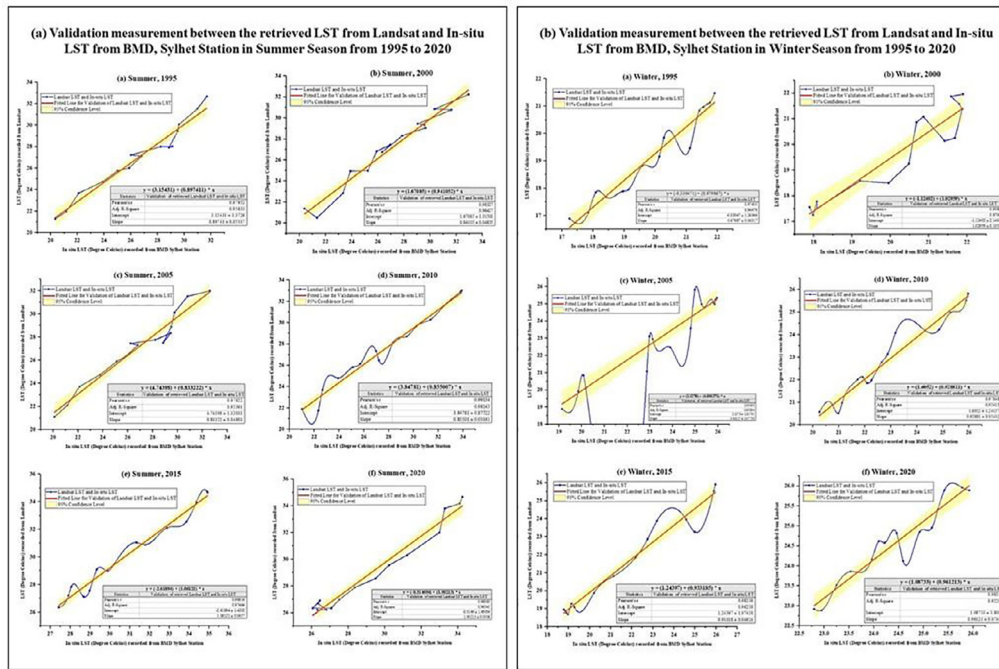


Fig. A.1 Validation measurement between retrieved Landsat and In-situ BMD Sylhet station LST data from 1995–2020 (a) Summer season; (b) Winter Season

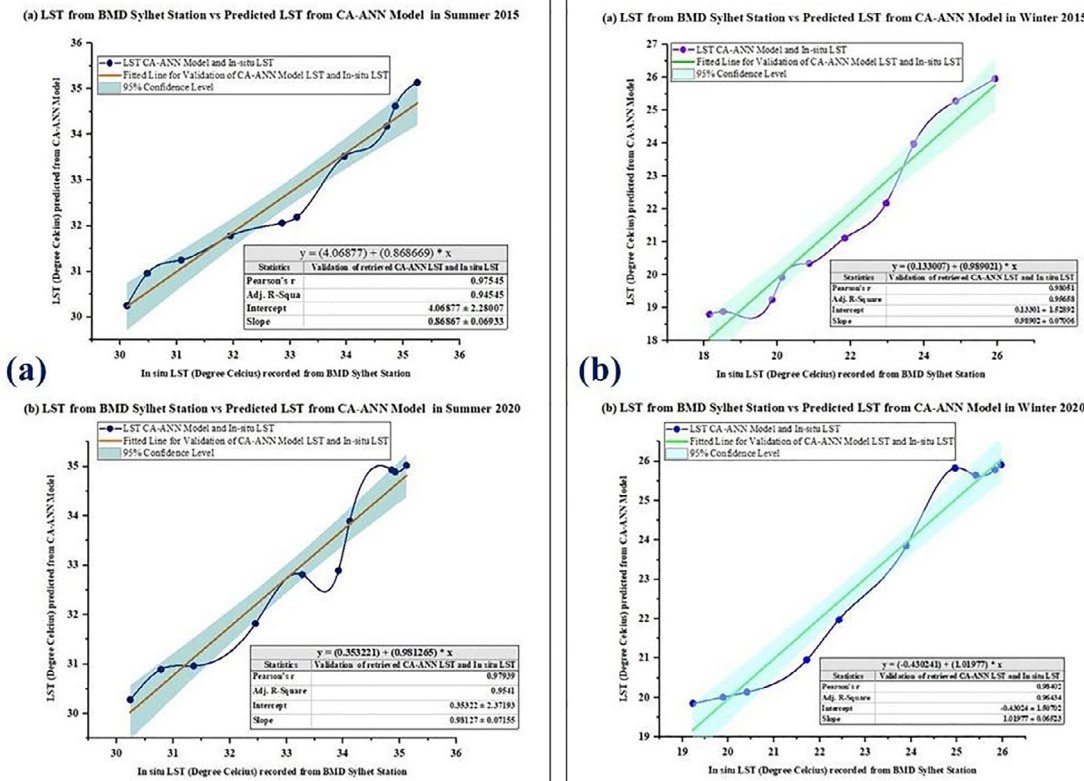


Fig. A.2 Validation measurement between predicted LST from CA-ANN and in-situ BMD Sylhet Station LST data for 2015 and 2020 (a) summer season; (b) winter Season

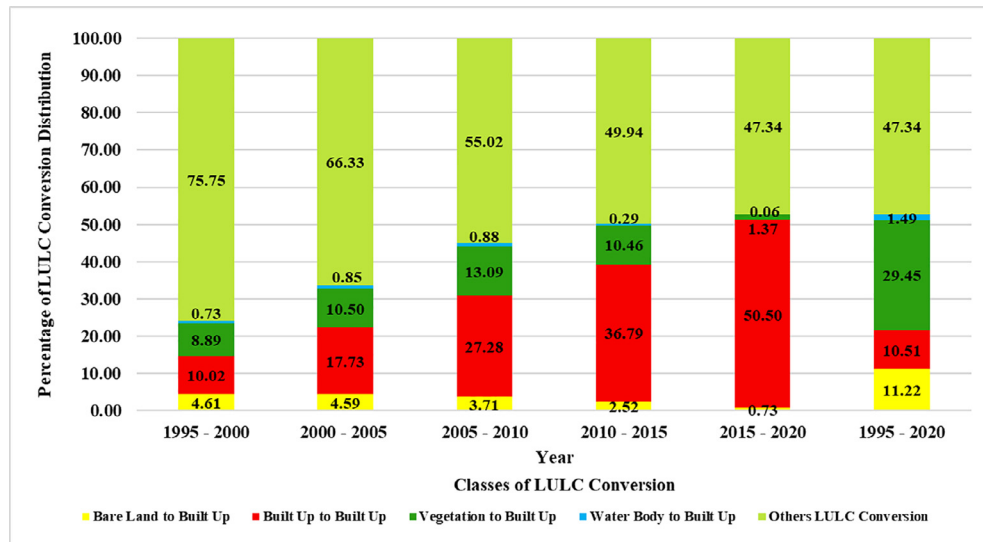


Fig. A.3 Conversion percentage of different land cover to built-up areas from 1995–2020

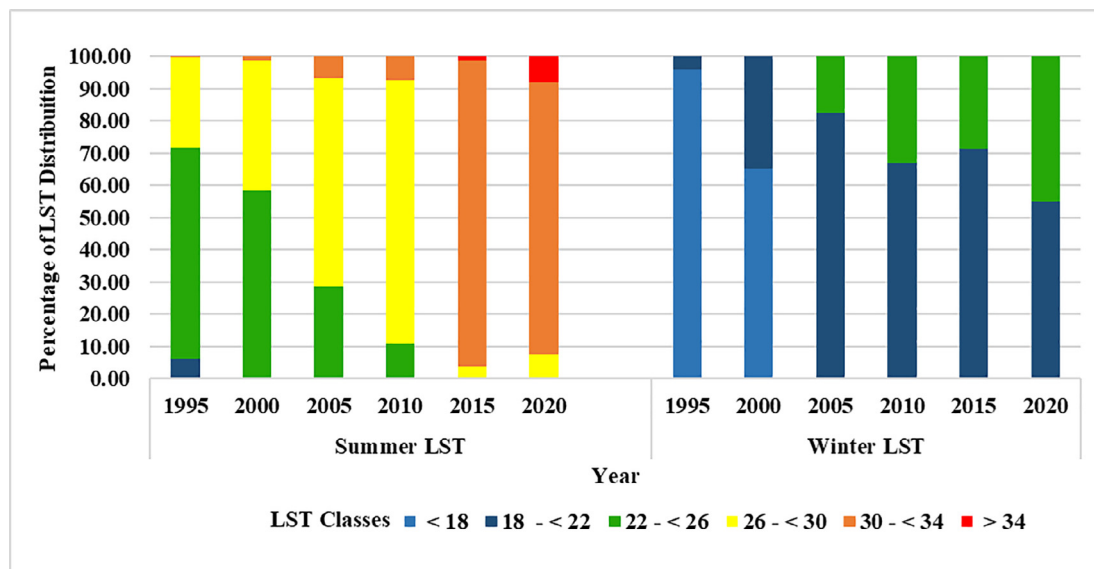


Fig. A.4 Percentage of LST Distribution in Summer and Winter Season

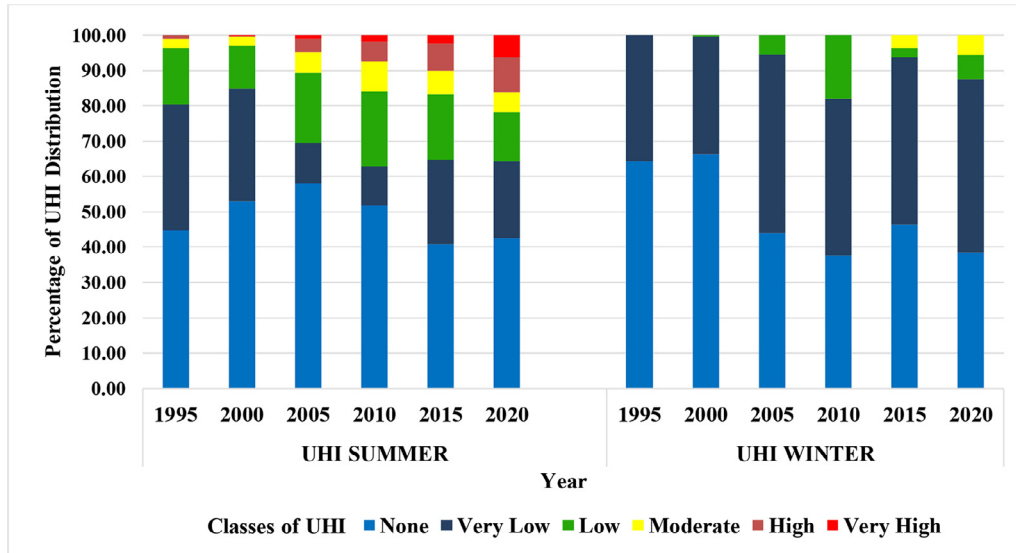


Fig. A.5 Percentage of UHI Distribution in Summer and Winter Season

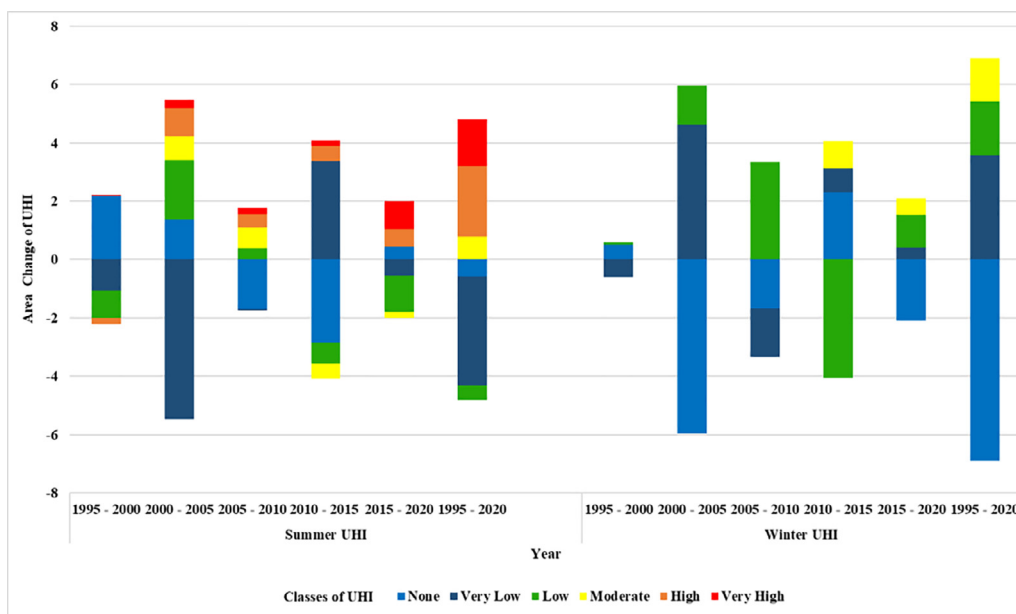
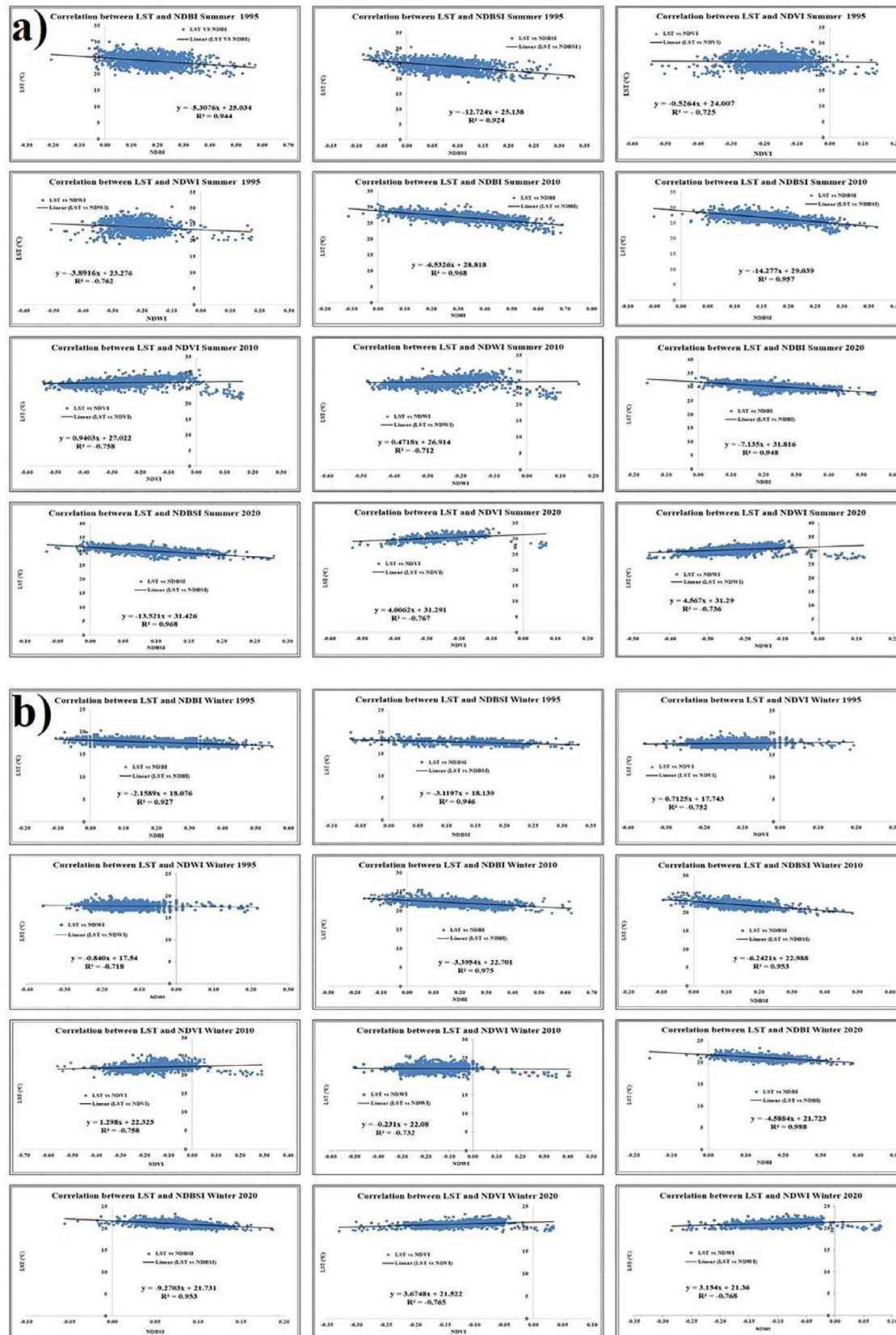


Fig. A.6 Area Change of UHI (Summer and Winter) from 1995 – 2020

**Fig. A.7** Correlation between a) summer and b) winter LST vs NDBI, NDVI, NDWI for years 1995, 2010, 2020

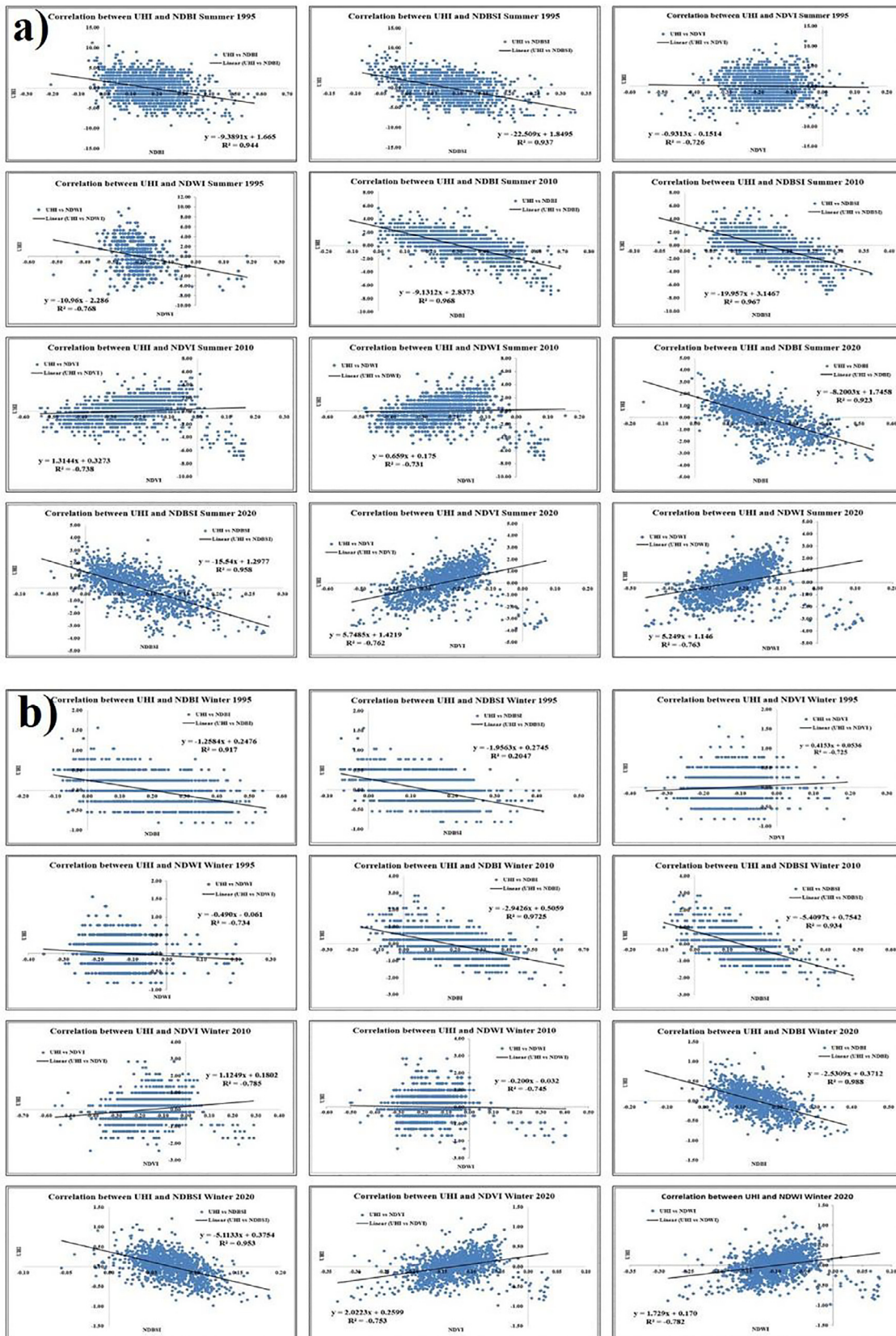


Fig. A.8 Correlation between a) summer and b) winter UHI vs NDBI, NDBSI, NDVI, NDWI for years 1995, 2010, 2020

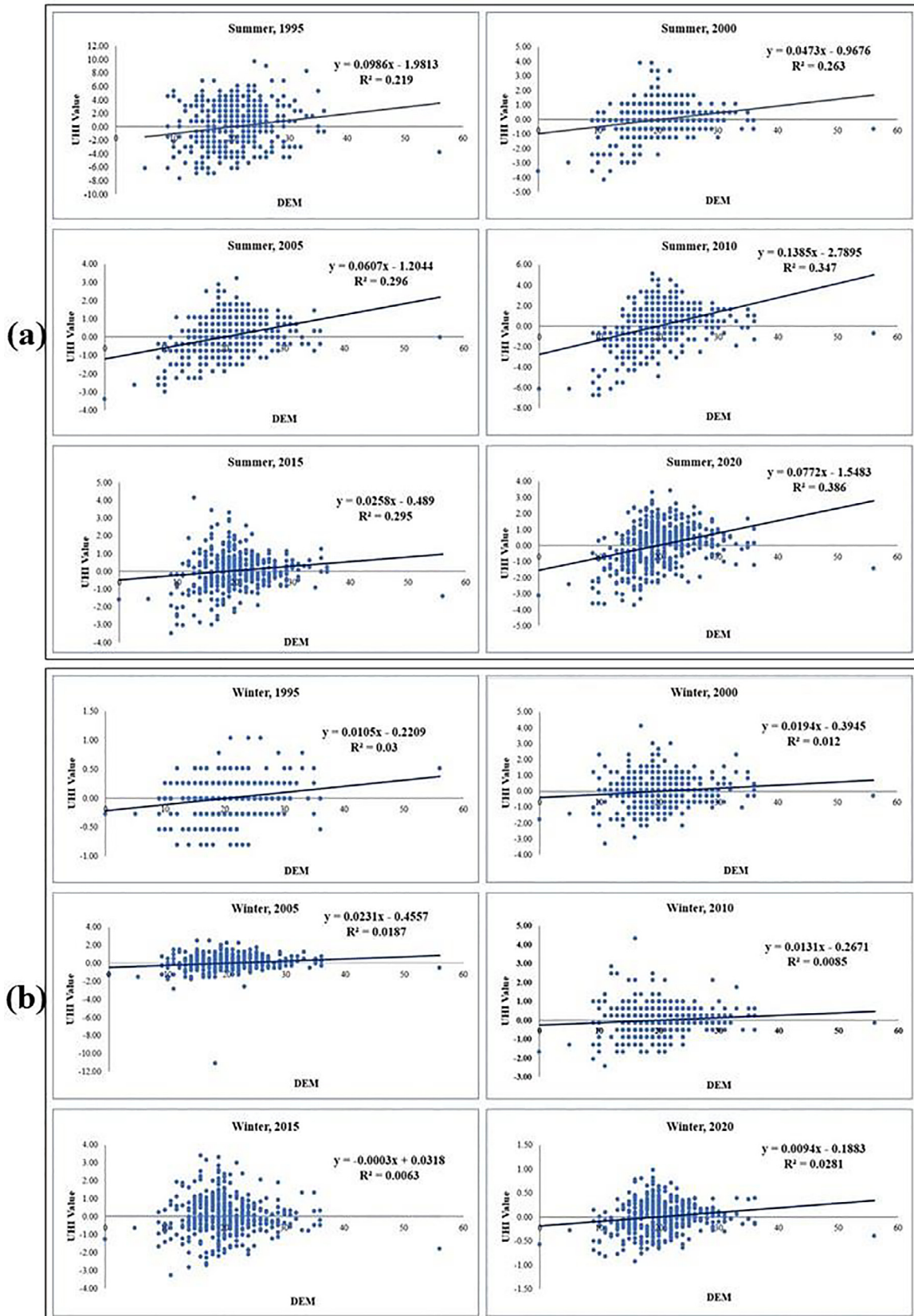


Fig. A.9 Correlation between (a) Summer and (b) Winter UHI and DEM from 1995 to 2015

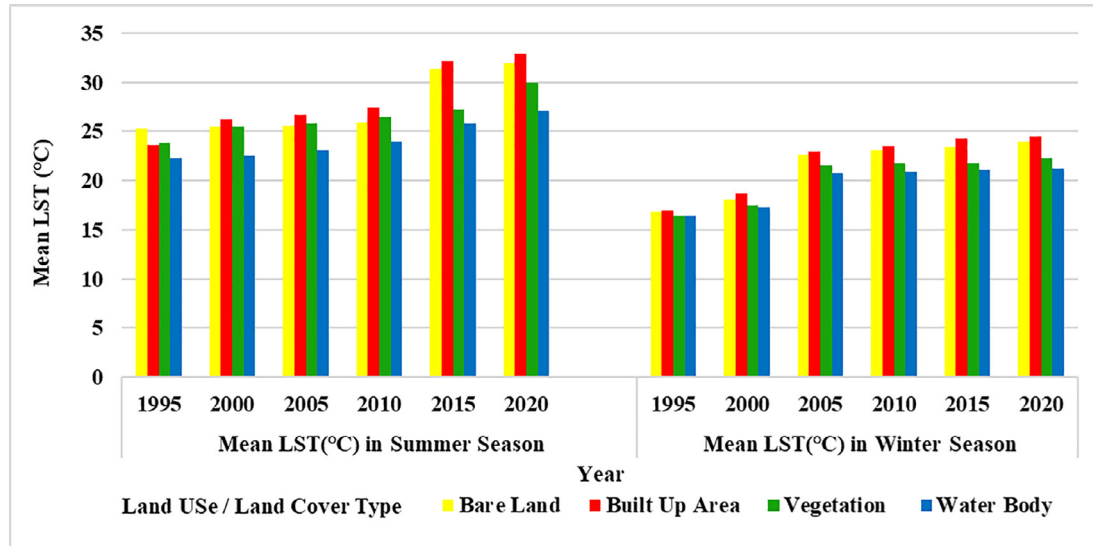


Fig. A.10 Mean LST (Summer and Winter) over different land cover for 1995, 2000, 2005, 2010, 2015, 2020

References

- [1] B. Cohen, Urbanization in developing countries: Current trends, future projections, and key challenges for sustainability, *Technol. Soc.* 28 (1–2) (2006) 63–80, <https://doi.org/10.1016/j.techsoc.2005.10.005>.
- [2] M.A. Hossain, R. Huggins, The Environmental and Social Impacts of Unplanned and Rapid Industrialization in Suburban Areas: The Case of the Greater Dhaka Region, Bangladesh, *Environ. Urban. ASIA* 12 (1) (2021) 73–89, <https://doi.org/10.1177/0975425321990319>.
- [3] “Sustainable Development Goals” UN, “UN, ‘Sustainable Development Goals,’ 2015,” 2015.
- [4] UN, “Goal 11: Make cities inclusive, safe, resilient and sustainable,” United Nations: Sustainable Development Goals, 2016.
- [5] M.M. Al-Humaiqani, S.G. Al-Ghamdi, The built environment resilience qualities to climate change impact: Concepts, frameworks, and directions for future research, *Sustain. Cities Soc.* 80 (2022), <https://doi.org/10.1016/j.scs.2022.103797>.
- [6] L. Mabon, K. Kondo, H. Kanekiyo, Y. Hayabuchi, A. Yamaguchi, Fukuoka: Adapting to climate change through urban green space and the built environment?, *Cities* 93 (2019) 273–285, <https://doi.org/10.1016/j.cities.2019.05.007>.
- [7] A. Aflaki et al., Urban heat island mitigation strategies: A state-of-the-art review on Kuala Lumpur, Singapore and Hong Kong, *Cities* 62 (2017) 131–145, <https://doi.org/10.1016/j.cities.2016.09.003>.
- [8] Z. Wu, Y. Ren, A bibliometric review of past trends and future prospects in urban heat island research from 1990 to 2017, *Environ. Rev.* 27 (2) (2019) 241–251, <https://doi.org/10.1139/er-2018-0029>.
- [9] Y.X. Ma, C. Yu, Impact of meteorological factors on high-rise office building energy consumption in Hong Kong: From a spatiotemporal perspective, *Energy Build.* 228 (2020), <https://doi.org/10.1016/j.enbuild.2020.110468>.
- [10] J. Schatz, C.J. Kucharik, Urban climate effects on extreme temperatures in Madison, Wisconsin, USA, *Environ. Res. Lett.* 10 (9) (2015) 94024, <https://doi.org/10.1088/1748-9326/10/9/094024>.
- [11] N. Huda, A. Kafy, Assessment of urban thermal field variance index and defining the relationship between land cover and surface temperature in Chattogram City: A remote sensing and statistical approach, *Environ. Challenges* 4 (March) (2021) 100107, <https://doi.org/10.1016/j.envc.2021.100107>.
- [12] M. Santamouris, C. Cartalis, A. Synnefa, D. Kolokotsa, On the impact of urban heat island and global warming on the power demand and electricity consumption of buildings—A review, *Energy Build.* 98 (2015) 119–124.
- [13] A. Dewan, G. Kiselev, D. Botje, G.I. Mahmud, M.H. Bhuiyan, Q.K. Hassan, Surface urban heat island intensity in five major cities of Bangladesh: Patterns, drivers and trends, *Sustain. Cities Soc.* 71 (2021), <https://doi.org/10.1016/j.scs.2021.102926> 102926.
- [14] P.A. Dugord, S. Lauf, C. Schuster, B. Kleinschmit, Land use patterns, temperature distribution, and potential heat stress risk – The case study Berlin, Germany, *Comput. Environ. Urban Syst.* 48 (2014) 86–98, <https://doi.org/10.1016/j.compenvurbsys.2014.07.005>.
- [15] Y. Zhang et al., Spatiotemporal characteristics of the surface urban heat island and its driving factors based on local climate zones and population in Beijing, China, *Atmosphere (Basel.)*, 12(10), 2021, doi: 10.3390/atmos12101271.
- [16] X. Li, Y. Zhou, G.R. Asrar, M. Imhoff, X. Li, The surface urban heat island response to urban expansion: A panel analysis for the conterminous United States, *Sci. Total Environ.* 605–606 (2017) 426–435, <https://doi.org/10.1016/j.scitotenv.2017.06.229>.
- [17] C. Ketterer, A. Matzarakis, Comparison of different methods for the assessment of the urban heat island in Stuttgart, Germany, *Int. J. Biometeorol.* 59 (9) (2015) 1299–1309, <https://doi.org/10.1007/s00484-014-0940-3>.
- [18] A. Khan and S. Chatterjee, “Numerical simulation of urban heat island intensity under urban–suburban surface and reference site in Kolkata, India,” *Model. Earth Syst. Environ.*, 2(2), 2016, doi: 10.1007/s40808-016-0119-5.
- [19] S. Arghavani, H. Malakooti, and A. A. Ali Akbari Bidokhti, “Numerical assessment of the urban green space scenarios on urban heat island and thermal comfort level in Tehran Metropolis,” *J. Clean. Prod.*, vol. 261, 2020, doi: 10.1016/j.jclepro.2020.121183.
- [20] M.A. Fattah, S.R. Morshed, S.Y. Morshed, Multi-layer perceptron-Markov chain-based artificial neural network for modelling future land-specific carbon emission pattern and its influences on surface temperature, *SN Appl. Sci.* 3 (3) (2021) 1–22, <https://doi.org/10.1007/s42452-021-04351-8>.
- [21] A. Al Kafy, A. Al Faisal, A. Al Rakib, M.A. Fattah, Z.A. Rahaman, G.S. Sattar, Impact of vegetation cover loss on surface temperature and carbon emission in a fastest-growing city, Cumilla, Bangladesh, *Build. Environ.* (2021), <https://doi.org/10.1016/j.buildenv.2021.108573>.
- [22] J. Mandal, P.P. Patel, S. Samanta, Examining the expansion of Urban Heat Island effect in the Kolkata Metropolitan Area and its vicinity using multi-temporal MODIS satellite data, *Adv. Sp. Res.* 69 (5) (2022) 1960–1977, <https://doi.org/10.1016/j.asr.2021.11.040>.
- [23] C. Yuan, A.S. Adelia, S. Mei, W. He, X.X. Li, L. Norford, Mitigating intensity of urban heat island by better understanding on urban morphology and anthropogenic heat dispersion, *Build. Environ.* 176 (2020), <https://doi.org/10.1016/j.buildenv.2020.106876>.
- [24] J. Ngarambe, J. Nganyiyimana, I. Kim, M. Santamouris, and G. Young Yun, “Synergies between urban heat island and heat waves in Seoul: The role of wind speed and land use characteristics,” *PLoS One*, 15(12 December), 2020, doi: 10.1371/journal.pone.0243571.
- [25] X. Li, Y. Zhou, S. Yu, G. Jia, H. Li, W. Li, Urban heat island impacts on building energy consumption: A review of approaches and findings, *Energy* 174 (2019) 407–419, <https://doi.org/10.1016/j.energy.2019.02.183>.

- [26] H. Louiza, A. Zéroual, H. Djamel, Impact of the Transport on the Urban Heat Island, *Int. J. Traffic Transp. Eng.* 5 (3) (2015) 252–263, [https://doi.org/10.7708/ijtte.2015.5\(3\).03](https://doi.org/10.7708/ijtte.2015.5(3).03).
- [27] C. Wang, S. W. Myint, Z. Wang, and J. Song, "Spatio-temporal modeling of the urban heat island in the Phoenix metropolitan area: Land use change implications," *Remote Sens.*, 8(3), 2016, doi: 10.3390/rs8030185.
- [28] A.-A. Faisal et al., Assessing and predicting land use/land cover, land surface temperature and urban thermal field variance index using Landsat imagery for Dhaka Metropolitan area, *Environ. Challenges* 4 (June) (2021) 100192, <https://doi.org/10.1016/j.envc.2021.100192>.
- [29] N. Samat, M.A. Mahamud, M.L. Tan, M.J.M. Tilaki, Y.L. Tew, Modelling land cover changes in peri-urban areas: A case study of George Town conurbation, Malaysia, *Land* 9 (10) (2020) 1–16, <https://doi.org/10.3390/land9100373>.
- [30] W. M. M. Al-Hameedi et al., "Remote sensing-based urban sprawl modeling using multilayer perceptron neural network markov chain in Baghdad, Iraq," *Remote Sens.*, 13(20), 2021, doi: 10.3390/rs13204034.
- [31] C. Losiri, M. Nagai, S. Ninsawat, R.P. Shrestha, Modeling urban expansion in Bangkok Metropolitan region using demographic-economic data through cellular automata-Markov Chain and multi-Layer perceptron-Markov chain models, *Sustainability* 8 (7) (2016) 686.
- [32] N. Shatnawi, H. Abu Qdais, Mapping urban land surface temperature using remote sensing techniques and artificial neural network modelling, *Int. J. Remote Sens.* 40 (10) (2019) 3968–3983, <https://doi.org/10.1080/01431161.2018.1557792>.
- [33] S. Gupta, S. Islam, M. Hasan, Analysis of impervious land-cover expansion using remote sensing and GIS: A case study of Sylhet Sadar Upazila, *Appl. Geogr.* 98 (July) (2018) 156–165, <https://doi.org/10.1016/j.apgeog.2018.07.012>.
- [34] "Sylhet Climate: Weather By Month, Average Temperature (Bangladesh) - Weather Spark." <https://weatherspark.com/y/111977/Average-Weather-in-Sylhet-Bangladesh-Year-Round> (accessed Aug. 20, 2022).
- [35] Z. Qiao, G. Tian, L. Zhang, X. Xu, Influences of urban expansion on urban heat island in Beijing during 1989–2010, *Adv. Meteorol.* 2014 (2014), <https://doi.org/10.1155/2014/187169>.
- [36] J.H. Xu, C.L. Fang, W.Z. Yue, An analysis of the mosaic structure of regional landscape using GIS and remote sensing, *Acta Ecol. Sin.* 23 (2) (2003) 365–375.
- [37] W. Kuang, S. Zhang, Y. Zhang, Y. Sheng, Analysis of urban land utilization spatial expansion mechanism in Changchun city since 1900, *Acta Geogr. Sin.* 60 (5) (2005) 841–850.
- [38] S.Q. Zhang, J.Y. Zhang, F. Li, Vector analysis theory on landscape pattern in Sanjiang plain marsh, China, *Wetl. Sci.* 9 (3) (2004) 161–170.
- [39] M. Aboelnour, B.A. Engel, Application of Remote Sensing Techniques and Geographic Information Systems to Analyze Land Surface Temperature in Response to Land Use/Land Cover Change in Greater Cairo Region, Egypt, *J. Geogr. Inf. Syst.* 10 (01) (2018) 57.
- [40] A.-A. Al Kafy et al., "Monitoring the effects of vegetation cover losses on land surface temperature dynamics using geospatial approach in Rajshahi City, Bangladesh", *Environ. Challenges* 4 (June) (2021) 100187, <https://doi.org/10.1016/j.envc.2021.100187>.
- [41] S. Anbazhagan, C.R. Paramasivam, Statistical correlation between land surface temperature (LST) and vegetation index (NDVI) using multi-temporal landsat TM data, *Int. J. Adv. Earth Sci. Eng.* 5 (1) (2016) 333–346.
- [42] S. Roy et al., Examining the nexus between land surface temperature and urban growth in Chatogram Metropolitan Area of Bangladesh using long term Landsat series data, *Urban Clim.* 32 (2020) 100593.
- [43] S. Ullah, K. Ahmad, R.U. Sajjad, A.M. Abbasi, A. Nazeer, A.A. Tahir, Analysis and simulation of land cover changes and their impacts on land surface temperature in a lower Himalayan region, *J. Environ. Manage.* 245 (2019) 348–357.
- [44] S. Guha, H. Govil, A. Dey, N. Gill, Analytical study of land surface temperature with NDVI and NDBI using Landsat 8 OLI and TIRS data in Florence and Naples city, Italy, *Eur. J. Remote Sens.* 51 (1) (2018) 667–678, <https://doi.org/10.1080/22797254.2018.1474494>.
- [45] S. Pal, S. Ziaul, Detection of land use and land cover change and land surface temperature in English Bazar urban centre, *Egypt. J. Remote Sens. Sp. Sci.* 20 (1) (2017) 125–145.
- [46] H.-Q. Xu, B.-Q. Chen, Remote sensing of the urban heat island and its changes in Xiamen City of SE China, *J. Environ. Sci.* 16 (2) (2004) 276–281.
- [47] H.Q. Xu, B.Q. Chen, An image processing technique for the study of urban heat island changes using different seasonal remote sensing data, *Remote Sens. Technol. Appl.* 18 (3) (2003) 129–133.
- [48] T.W. Hawkins, A.J. Brazel, W.L. Stefanov, W. Bigler, E.M. Saffell, The role of rural variability in urban heat island determination for Phoenix, Arizona, *J. Appl. Meteorol.* 43 (3) (2004) 476–486.
- [49] D.R. Streutker, A remote sensing study of the urban heat island of Houston, Texas, *Int. J. Remote Sens.* 23 (13) (2002) 2595–2608.
- [50] H. Cao, J. Liu, J. Chen, J. Gao, G. Wang, W. Zhang, Spatiotemporal Patterns of Urban Land Use Change in Typical Cities in the Greater Mekong Subregion (GMS), *Remote Sens.* 11 (7) (2019) 801.
- [51] A. Al Kafy et al., "Prediction of seasonal urban thermal field variance index using machine learning algorithms in Cumilla, Bangladesh," *Sustain. Cities Soc.*, 64(September 2020), p. 102542, 2021, doi: 10.1016/j.scs.2020.102542.
- [52] A. Al et al., Predicting the impacts of land use / land cover changes on seasonal urban thermal characteristics using machine learning algorithms, *Build. Environ.* 217 (February) (2022) 109066, <https://doi.org/10.1016/j.buildenv.2022.109066>.
- [53] E. Buğday, S. Erkan Büğday, Modeling and simulating land use/cover change using artificial neural network from remotely sensing data, *Cerne* 25 (2) (2019) 246–254, <https://doi.org/10.1590/01047760201925022634>.
- [54] U.E. Msovu, D.M.M. Mulungu, J.K. Nobert, H. Mahoo, Land Use/Cover Change and their Impacts on Streamflow in Kikuletwa Catchment of Pangani River Basin, Tanzania, *Tanzania J. Eng. Technol.* 38 (2) (2019) 171–192, <https://doi.org/10.52339/tjet.v38i2.503>.
- [55] A. M. Y. Hakim, S. Baja, D. A. Rampisela, and S. Arif, "Spatial dynamic prediction of landuse / landcover change (case study: Tamalanrea sub-district, makassar city)," in IOP Conference Series: Earth and Environmental Science, 2019, vol. 280, no. 1, doi: 10.1088/1755-1315/280/1/012023.
- [56] E.D. Ashaolu, J.F. Olorunfemi, I.P. Ifabiyi, Assessing the Spatio-Temporal Pattern of Land Use and Land Cover Changes in Osun Drainage Basin, Nigeria, *J. Environ. Geogr.* 12 (1–2) (2019) 41–50, <https://doi.org/10.2478/jengeo-2019-0005>.
- [57] M.T.U. Rahman et al., Temporal dynamics of land use/land cover change and its prediction using CA-ANN model for southwestern coastal Bangladesh, *Environ. Monit. Assess.* 189 (11) (2017) 1–18.
- [58] A.M. El-Tantawi, A. Bao, C. Chang, Y. Liu, Monitoring and Predicting Land Use/ Cover Changes in the Aksu - Tarim River Basin, Xinjiang - China (1990–2030), *Environ. Monit. Assess.* 191 (2019) 1–18, <https://doi.org/10.1007/s10661-019-7478-0>.
- [59] M.L.G. Guidingan, C.L. Sanou, D.S. Ragatoa, C.O. Fafa, V.N. Mishra, Assessing Land Use/Land Cover Dynamic and Its Impact in Benin Republic Using Land Change Model and CCI-LC Products, *Earth Syst. Environ.* 3 (2019) 127–137, <https://doi.org/10.1007/s41748-018-0083-5>.
- [60] R.K. Bhattacharya, N. Das Chatterjee, K. Das, Land use and Land Cover change and its resultant erosion susceptible level: an appraisal using RUSLE and Logistic Regression in a tropical plateau basin of West Bengal, India, *Environ. Dev. Sustain.* 23 (2) (2021) 1411–1446, <https://doi.org/10.1007/s10668-020-00628-x>.
- [61] J.N. Mandrekar, Receiver Operating Characteristic Curve in Diagnostic Test Assessment, *J. Thorac. Oncol.* 5 (9) (2010) 1315–1316, <https://doi.org/10.1097/JTO.0b013e3181ec173d>.
- [62] W.-S. Lee, S.-G. Jung, The application of a prediction model on land surface temperature using Artificial Neural Network and Scenario: Focused on Changwon in South Korea, *J. Korean Planners Assoc.* 49 (1) (2014) 263, <https://doi.org/10.17208/jkpa.2014.02.49.1.263>.
- [63] I.D. Maduako, Z. Yun, B. Patrick, Simulation and prediction of land surface temperature (LST) dynamics within Ikom City in Nigeria using artificial neural network (ANN), *J. Remote Sens. GIS* 5 (1) (2016) 1–7.
- [64] M. Van Gerven, S. Bohte, Artificial neural networks as models of neural information processing, *Front. Comput. Neurosci.* 11 (2017) 114.
- [65] A. Sekertekin, N. Arslan, M. Bilgili, Modeling Diurnal Land Surface Temperature on a Local Scale of an Arid Environment Using Artificial Neural Network (ANN) and Time Series of Landsat-8 Derived Spectral Indexes, *J. Atmos. Solar-Terrestrial Phys.* 206 (2020), <https://doi.org/10.1016/j.jastp.2020.105328>.
- [66] A. Sekertekin and S. Bonafoni, "Land surface temperature retrieval from Landsat 5, 7, and 8 over rural areas: Assessment of different retrieval algorithms and emissivity models and toolbox implementation," *Remote Sens.*, 12(2), 2020, doi: 10.3390/rs12020294.
- [67] M. Bilgili, The use of artificial neural networks for forecasting the monthly mean soil temperatures in Adana, Turkey, *Turkish J. Agric. For.* 35 (1) (2011) 83–93, <https://doi.org/10.3906/tar-1001-593>.
- [68] P. Kumar, D.K. Gupta, V.N. Mishra, R. Prasad, Comparison of support vector machine, artificial neural network, and spectral angle mapper algorithms for crop classification using LISS IV data, *Int. J. Remote Sens.* 36 (6) (2015) 1604–1617.
- [69] V. Anand, B. Oinam, Future land use land cover prediction with special emphasis on urbanization and wetlands, *Remote Sens. Lett.* 11 (3) (2020) 225–234, <https://doi.org/10.1080/2150704X.2019.1704304>.
- [70] K. Gardner, International migration and the rural context in sylhet, *J. Ethn. Migr. Stud.* 18 (4) (1992) 579–590, <https://doi.org/10.1080/1369183X.1992.9976331>.
- [71] M.F. Ahmed, M.S. Islam, Urbanization and Environmental Problem: An Empirical Study, *J. Int. Inst. Sci. Technol. Educ.* 4 (3) (2014) 161–172.
- [72] K. Abutaleeb, A. Ngie, A. Darwish, M. Ahmed, S. Arafat, F. Ahmed, Assessment of Urban Heat Island Using Remotely Sensed Imagery over Greater Cairo, Egypt, *Adv. Remote Sens.* 04 (01) (2015) 35–47, <https://doi.org/10.4236/ars.2015.41004>.
- [73] Q. Huang, J. Huang, X. Yang, C. Fang, Y. Liang, Quantifying the seasonal contribution of coupling urban land use types on Urban Heat Island using Land Contribution Index: A case study in Wuhan, China, *Sustain. Cities Soc.* 44 (2019) 666–675.
- [74] T. R. Karl, S. J. Hassol, C. D. Miller, and W. L. Murray, "Temperature Trends in the Lower Atmosphere Steps for Understanding and Reconciling Differences," Program, vol. 17, no. April, p. 180, 2006, [Online]. Available: <http://www.climatescience.gov/Library/sap/sap1-1/finalreport/default.htm>.
- [75] M. Roth, T.R. Oke, W.J. Emery, Satellite-derived urban heat islands from three coastal cities and the utilization of such data in urban climatology, *Int. J. Remote Sens.* 10 (11) (1989) 1699–1720, <https://doi.org/10.1080/01431168908904002>.

- [76] P. Zhang, L. Bounoua, M.L. Imhoff, R.E. Wolfe, K. Thome, Comparison of MODIS Land Surface Temperature and Air Temperature over the Continental USA Meteorological Stations, *Can. J. Remote Sens.* 40 (2) (2014) 110–122, <https://doi.org/10.1080/07038992.2014.935934>.
- [77] M. Urban, J. Eberle, C. Hüttich, C. Schmullius, M. Herold, Comparison of satellite-derived land surface temperature and air temperature from meteorological stations on the pan-arctic scale, *Remote Sens.* 5 (5) (2013) 2348–2367, <https://doi.org/10.3390/rs5052348>.
- [78] Z. Wan, Y. Zhang, Q. Zhang, Z.L. Li, Quality assessment and validation of the MODIS global land surface temperature, *Int. J. Remote Sens.* 25 (1) (2004) 261–274, <https://doi.org/10.1080/0143116031000116417>.
- [79] D.J. Mildrexler, M. Zhao, S.W. Running, A global comparison between station air temperatures and MODIS land surface temperatures reveals the cooling role of forests, *J. Geophys. Res. Biogeosciences* 116 (3) (2011) 1–15, <https://doi.org/10.1029/2010JG001486>.
- [80] A. Al Kafy et al., “I P re,” *Sustain. Cities Soc.*, p. 102542, 2020, doi: 10.1016/j.scs.2020.102542.
- [81] K.H. Yim, F.S. Nahm, K.A. Han, S.Y. Park, *Analysis of Statistical Methods and Errors in the Articles Published in the Korean J. Pain* 23 (1) (2010) 35–41.
- [82] A. Rasul and R. Ningthoujam, “Snow cover and vegetation greenness with leaf water content control the global land surface temperature,” *Environ. Dev. Sustain.*, no. 0123456789, 2021, doi: 10.1007/s10668-021-01269-4.
- [83] M. E. Awuh, P. O. Japhets, M. C. Officha, A. O. Okolie, and I. C. Enete, “A Correlation Analysis of the Relationship between Land Use and Land Cover / Land Surface Temperature in Abuja Municipal ,” pp. 44–55, 2019, doi: 10.4236/jgis.2019.111004.
- [84] B. Onwuka, Effects of Soil Temperature on Some Soil Properties and Plant Growth, *Adv. Plants Agric. Res.* 8 (1) (2018) 34–37, <https://doi.org/10.15406/apar.2018.08.00288>.
- [85] L. Wang, J. Zhu, Y. Xu, and Z. Wang, “Urban built-up area boundary extraction and spatial-temporal characteristics based on land surface temperature retrieval,” *Remote Sens.*, 10(3), 2018, doi: 10.3390/rs10030473.
- [86] S. Pramanik, M. Punia, Land use/land cover change and surface urban heat island intensity: source-sink landscape-based study in Delhi, India, *Environ. Dev. Sustain.* 22 (8) (2020) 7331–7356, <https://doi.org/10.1007/s10668-019-00515-0>.
- [87] S. Sen, J. Roesler, B. Ruddell, A. Middel, Cool pavement strategies for Urban Heat Island mitigation in Suburban Phoenix, Arizona, *Sustain.* 11 (16) (2019) 1–21, <https://doi.org/10.3390/su11164452>.
- [88] H. Akbari, M. Pomerantz, H. Taha, Cool Surfaces and Shade Trees to Reduce Energy Use and Improve Air Quality in Urban Areas, *Sol. Energy* 70 (3) (2001) 295–310, [https://doi.org/10.1016/S0038-092X\(00\)00089-X](https://doi.org/10.1016/S0038-092X(00)00089-X).
- [89] F. Rossi, A.L. Pisello, A. Nicolini, M. Filipponi, M. Palombo, Analysis of retro-reflective surfaces for urban heat island mitigation: A new analytical model, *Appl. Energy* 114 (2014) 621–631, <https://doi.org/10.1016/j.apenergy.2013.10.038>.
- [90] H. Takebayashi, M. Moriyama, Study on surface heat budget of various pavements for urban heat island mitigation, *Adv. Mater. Sci. Eng.* 2012 (July) (2012), <https://doi.org/10.1155/2012/523051>.
- [91] N. Debbage, J.M. Shepherd, The urban heat island effect and city contiguity, *Comput. Environ. Urban Syst.* 54 (2015) 181–194, <https://doi.org/10.1016/j.compenvurbsys.2015.08.002>.
- [92] A. Mohajerani, J. Bakaric, T. Jeffrey-Bailey, The urban heat island effect, its causes, and mitigation, with reference to the thermal properties of asphalt concrete, *J. Environ. Manage.* 197 (2017) 522–538, <https://doi.org/10.1016/j.jenvman.2017.03.095>.
- [93] L. Doulos, M. Santamouris, I. Livada, Passive cooling of outdoor urban spaces. The role of materials, *Sol. Energy* 77 (2) (2004) 231–249, <https://doi.org/10.1016/j.solener.2004.04.005>.
- [94] B. Stone, J.J. Hess, H. Frumkin, Urban form and extreme heat events: Are sprawling cities more vulnerable to climate change than compact cities?, *Environ Health Perspect.* 118 (10) (2010) 1425–1428, <https://doi.org/10.1289/ehp.0901879>.
- [95] M. Santamouris, Using cool pavements as a mitigation strategy to fight urban heat island - A review of the actual developments, *Renew. Sustain. Energy Rev.* 26 (2013) 224–240, <https://doi.org/10.1016/j.rser.2013.05.047>.
- [96] S. Grimmond, Urbanization and global environmental change: Local effects of urban warming, *Geogr. J.* 173 (1) (2007) 83–88, https://doi.org/10.1111/j.1475-4959.2007.0232_3.x.
- [97] A. Hesaraki, S. Holmberg, F. Haghhighat, Seasonal thermal energy storage with heat pumps and low temperatures in building projects - A comparative review, *Renew. Sustain. Energy Rev.* 43 (2015) 1199–1213, <https://doi.org/10.1016/j.rser.2014.12.002>.
- [98] X. Peng, W. Wu, Y. Zheng, J. Sun, T. Hu, P. Wang, Correlation analysis of land surface temperature and topographic elements in Hangzhou, China, *Sci. Rep.* 10 (1) (2020) 1–16, <https://doi.org/10.1038/s41598-020-67423-6>.
- [99] A. Mathew, S. Khadelwal, N. Kaul, Spatial and temporal variations of urban heat island effect and the effect of percentage impervious surface area and elevation on land surface temperature: Study of Chandigarh city, India, *Sustain. Cities Soc.* 26 (2016) 264–277, <https://doi.org/10.1016/j.scs.2016.06.018>.
- [100] K.R. Gunawardena, M.J. Wells, T. Kershaw, Utilising green and bluespace to mitigate urban heat island intensity, *Sci. Total Environ.* 584–585 (2017) 1040–1055, <https://doi.org/10.1016/j.scitotenv.2017.01.158>.
- [101] C. P. Lo and D. A. Quattrochi, “Urban Heat Island Phenomenon , and Health Implications : A Remote Sensing Approach,” 69(9), pp. 1053–1063, 2003.
- [102] L. Cover, “Surface Urban Heat Island Analysis of Shanghai (China) Based on the Change of Land Use and,” 2017, doi: 10.3390/su9091538.
- [103] M.S. Hossain et al., Climate change impacts on farmland value in Bangladesh, *Ecol. Indic.* 112 (January) (2020) 106181, <https://doi.org/10.1016/j.ecolind.2020.106181>.
- [104] D. C.-G. Kim, “The Impact of Climate Change on the Agricultural Sector : Implications of the Agro - Industry for Low Carbon , Green Growth Strategy and Roadmap for the East Asian Region Table of Contents,” 2008.
- [105] D. R. Streutker, “Satellite-measured growth of the urban heat island of Houston , Texas,” vol. 85, pp. 282–289, 2003, doi: 10.1016/S0034-4257(03)00007-5.
- [106] X. Yang, L.L.H. Peng, Z. Jiang, Y. Chen, L. Yao, Y. He, Impact of urban heat island on energy demand in buildings: Local climate zones in Nanjing, *Appl. Energy* 260 (30) (2020), <https://doi.org/10.1016/j.apenergy.2019.114279> 114279.
- [107] M. Santamouris, “Recent progress on urban overheating and heat island research: integrated assessment of the energy, environmental, vulnerability and health impact synergies with the global climate change,” no. xxxx, 2019, doi: 10.1016/j.enbuild.2019.109482.
- [108] A.I. Almulhim, Understanding public awareness and attitudes toward renewable energy resources in Saudi Arabia, *Renewable Ener.* (2022) 572–582, <https://doi.org/10.1016/j.renene.2022.04.122>, In this issue.
- [109] Almulhim, Ismaila Rimi Abubakar, Understanding Public Environmental Awareness and Attitudes toward Circular Economy Transition in Saudi Arabia, *Sustainability* (2021), <https://doi.org/10.3390/su131810157>.